



# Università di Genova

UNIVERSITÀ DEGLI STUDI DI GENOVA

PHD IN MARINE AND SCIENCE TECHNOLOGIES

CURRICULUM: MARINE AND NAUTICAL ENGINEERING,  
MARINE TECHNOLOGIES

XXXVII CYCLE

---

**Computer Vision Techniques in Cavitation Studies**

---

*Candidate:*  
Giovanni Franzosi

*Supervisor:*  
Prof. Giorgio Tani

*After an opinion from:*  
External reviewers

*In front of a jury composed of:*  
Jury members

*Date:*  
To be defined



# Abstract

Collecting experimental data is of considerable importance in the study of cavitation. Indeed, empirical methods are often used in the design of ship propellers. In this scenario, acquiring a deeper and more detailed knowledge of cavitation phenomena would allow a more comprehensive understanding of their effects and risks and, therefore, a more efficient design.

This thesis presents an approach based on computer vision techniques for studying cavitation. Specifically, the research focuses on analyzing the dynamics of cavitating structures and their influence on cavitation-related effects, such as underwater radiated noise and cavitation erosion. To this end, two distinct case studies were considered. For each case, the proposed approach demonstrated that applying computer vision to the study of cavitation provides valuable data that are otherwise challenging or impossible to obtain. Furthermore, combining the information derived from computer vision algorithms with the time resolution offered by high-speed video recordings allows for quantitative observation of the dynamics of cavitation phenomena.

This kind of data provides valuable information, whether for estimating a phenomenon's erosive potential or predicting the produced acoustic radiation. Unfortunately, using these techniques in conventional tests conducted in cavitation tunnels is not straightforward due to various environmental factors that significantly complicate measurements. For this reason, the thesis details the method's development, showing the challenges encountered and the solutions adopted at each stage. The resulting method proved robust and adaptable to different scenarios with a moderate level of effort. It enabled the collection of detailed measurements of cavitation and its dynamics, paving the way for new and insightful studies.



# Contents

<b>Abstract</b>	iii
<b>List of Figures</b>	vii
<b>List of Tables</b>	ix
<b>1 Introduction</b>	1
1.1 Background . . . . .	1
1.2 Scientific Gap and Thesis Aims . . . . .	2
1.3 Thesis Layout . . . . .	3
<b>2 Cavitation Fundamentals</b>	5
2.1 General Aspects . . . . .	5
2.2 Types of Cavitation . . . . .	7
2.2.1 Bubble Cavitation . . . . .	7
2.2.2 Sheet Cavitation . . . . .	9
2.2.3 Cloud Cavitation . . . . .	11
2.2.4 Vortex Cavitation . . . . .	12
<b>3 Main effects of cavitation on marine propellers</b>	15
3.1 Cavitation Erosion . . . . .	15
3.1.1 Theory and Modeling Approaches . . . . .	16
3.1.2 Experimental Approaches for Cavitation Erosion . . . . .	17
3.2 Cavitation Underwater Radiated Noise . . . . .	20
3.2.1 Theory and Modeling Approaches . . . . .	20
3.2.2 Practical Noise Prediction . . . . .	22
3.3 Summary . . . . .	24
<b>4 Computer Vision in Cavitation Tunnel Environment</b>	25
4.1 Camera Model . . . . .	25
4.1.1 Pinhole Camera Model . . . . .	26
4.1.1.1 Omogeneous Coordinates . . . . .	27
4.1.1.2 General Camera Model . . . . .	28
4.1.2 Distortion Models . . . . .	31
4.1.2.1 Radial Distortion . . . . .	31
4.1.2.2 Tangential Distortion . . . . .	32
4.1.2.3 Thin-Prism Distortion . . . . .	33
4.1.2.4 Scheimpflug Principle . . . . .	33
4.1.2.5 Practical Applications . . . . .	34

---

4.1.3	Refraction Effects and Management . . . . .	35
4.2	Camera Calibration . . . . .	37
4.2.1	Mono Calibration . . . . .	38
4.2.1.1	Theoretical Aspects . . . . .	39
4.2.1.2	Accuracy Validation . . . . .	42
4.2.1.3	Warp Correction of Tunnel Windows . . . . .	43
4.2.2	Stereo Calibration . . . . .	46
4.2.2.1	Epioplar Geometry . . . . .	46
4.2.2.2	Theoretical Aspects . . . . .	49
4.2.2.3	Accuracy Validation . . . . .	50
4.2.3	Multiview Calibration . . . . .	53
4.2.3.1	Epioplar Graph . . . . .	54
4.2.3.2	Theoretical Aspects . . . . .	55
4.2.3.3	Accuracy Validation . . . . .	58
4.3	Recostruction Strategies . . . . .	59
4.3.1	Stereo Triangulation . . . . .	59
4.3.2	Shape from Silhouette . . . . .	62

# List of Figures

2.1	Water Phase Diagram (Carlton 2018) . . . . .	6
2.2	Van der Waals' isotherm and definition of tensile strength of liquid (Carlton 2018) . . . . .	6
2.3	Instability of the liquid layer under a traveling cavitation bubble (C.E. Brennen 2014) . . . . .	8
2.5	Bubble cavitation on a NACA 0015 hydrofoil for different cavitation number conditions . . . . .	9
2.7	Cloud cavitation on a NACA 0015 hydrofoil: production of cloud cavitation downstream of sheet cavitation (left) and downstream of travelling bubble cavitation (right). . . . .	11
2.8	Stable sheet cavitation on the suction side of a propeller blade (G. Kuiper 1998). . . . .	12
2.9	Cloud cavitation produced by vortex bursting on a full scale propeller Carlton 2018. . . . .	13
2.10	Cloudy cavitation structure resulting from the rebound of a collapsing cavity at the root of a propeller blade. . . . .	13
4.1	Refraction at air-plexiglass-water interface (Sedlazeck and Koch 2012). . . . .	26
4.2	Pinhole Camera Model . . . . .	27
4.3	Pinhole perspective projection mechanism. . . . .	27
4.4	Characteristic References Frames in the Pinhole Camera Model . . . . .	29
4.7	Characteristic angles of the Scheimpflug principle. . . . .	34
4.8	Refraction effect depending on the angle between the camera sensor and the air-water interface. Camera sensor parallel to air-water interface (Effect on Focal Length). . . . .	36
4.9	Refraction effect depending on the angle between the camera sensor and the air-water interface. Camera sensor non parallel to air-water interface (Effect on Principal Point). . . . .	36
4.10	Plexiglas prism. . . . .	37
4.12	Chessboard Corners detected in a Calibration Pattern . . . . .	39
4.13	Positioning of World Reference Frame on a Calibration Pattern . . . . .	40
4.14	Mean Reprojection Error per Distortion Model (Table 4.1) . . . . .	42
4.15	Focal Lengths Difference per Distortion Model (Table 4.1) . . . . .	42
4.16	Principal Point Difference per Distortion Model (Table 4.1) . . . . .	43
4.17	Measurement of the Tunnel Window Deformation . . . . .	44
4.18	Epipolar Geometry Elements . . . . .	47
4.19	Relationship between Stereo Camera Reference Frames . . . . .	48
4.20	Relative Orientation between Cameras and World Reference Frames	50

4.21 Mono and Stereo RMS Reprojection Error per Distortion Model (Table 4.1) . . . . .	51
4.22 Distribution of Percentage Triangulation Error per Distortion Model (Table 4.1) . . . . .	52
4.23 Relationship between Cameras in a Multicamera System . . . . .	54
4.24 Epipolar Graph Graphical Representation . . . . .	54
4.25 Statistical Distributions of Distances between Triangulated Homologous Points with Different Stereo Rigs . . . . .	59
4.26 Stereo Triangulation by Visual Beams Intersection . . . . .	60
4.27 Visual Cones Intersection in Shape by Silhouette . . . . .	63

# List of Tables

4.1	Combinations of distortion models considered . . . . .	35
4.2	Materials Refractive Indices . . . . .	35
4.3	Mean Errors in Warp Correction of Tunnel Windows. . . . .	45
4.4	Statistical Metrics for Different Distortion Models. Metrics include mean, maximum value, standard deviation (Std. Dev.), skewness, kurtosis, and percentage of outliers. . . . .	53
4.5	Triangulation Metrics for both the Stereo Rig in a Multiview Calibration . . . . .	58
4.6	Metrics of Distributions of Distances between Triangulated Homologous Points with Different Stereo Rig Configurations . . . . .	59



# Chapter 1

## Introduction

### 1.1 Background

Cavitation is a widely studied phenomenon in fluid dynamics. It occurs when the fluid breaks due to pressure conditions to form a vapour-filled cavity. In marine engineering applications, these cavities can present complex dynamics and produce very different phenomena, including bubble, sheet, cloud, and vortex cavitation. Each of these phenomena, which will be discussed in more detail below, forms and evolves with different mechanisms and has different implications on the hydrodynamic components on which it occurs. In marine engineering, cavitation poses critical challenges, especially for ship propellers and hull appendages. When cavitation occurs, the continuous collapses of vapour cavities may lead to material erosion. Cavitation erosion is mainly driven by high stress due to cavity collapses, which induce high-speed micro-jets and shockwaves. Repeated over time, these actions degrade material integrity, shortening the propeller's lifespan and demanding frequent repariments. Moreover, the pulsation and collapse of cavitation bubbles are a primary source of underwater noise, disrupting marine ecosystems, especially in areas with high traffic, where propeller cavitation noise becomes a major environmental pollutant. In addition to physical damage and noise, cavitation also reduces the hydrodynamic components' performances. For instance, under severe cavitation, the pressure distribution over the blades of a marine propeller significantly differs from the design one, leading to thrust breakdown and loss of efficiency. Therefore, due to cavitation, ships can experience vibrations and performance losses, which pose safety risks and increase operational costs due to higher fuel consumption.

In this scenario, avoiding cavitation appears to be an effective solution to address these issues. However, this approach is generally not practicable. Indeed, most solutions adopted to mitigate cavitation often result in compromised efficiency. For instance, modifying the pitch or shape of the blades may reduce cavitation but could simultaneously decrease the propeller's thrust-generating capability.

To achieve an optimal balance between cavitation reduction and high efficiency in hydrodynamic component design is necessary to deeply investigate mechanisms and dynamics of cavitation. Thus, developing experimental technique or numerical simulation is extremely important to gain the knowledge required to predict and control of cavitation-related effects.

## 1.2 Scientific Gap and Thesis Aims

In this regard, this study primarily focuses on cavitation erosion and cavitation-induced noise, as these two phenomena are often the most critical impacts of cavitation. Furthermore, studying these effects provides a foundation for understanding other detrimental consequences of cavitation. For instance, noise often correlates with vibration or pressure pulses. The scientific literature provides a broad spectrum of methodologies for analyzing these effects. These researchs, along with a comprehensive overview of the most advanced and sophisticated techniques, will be discussed in a dedicated chapter. However, to establish a clear foundation for this study's objectives, the following section presents standard practices and methodologies used to investigate and predict these phenomena.

Focusing on cavitation erosion, different approaches are available to get information regarding the aggressiveness of cavitation flow in terms of erosion potential or, more precisely, damage rate. Unfortunately, experimental and numerical approaches commonly employed in the study of erosive cavitation present several limitations. Numerical methods for erosion risk assessment can generally be divided into two groups. The first group does not resolve the dynamics of individual cavities and their collapse; instead, it relies on mixture theory. These methods generally estimate the cavitation erosive power using aggressiveness criteria based on specific parameters, often necessitating empirical calibration. The second group methods provides a more comprehensive description of cavitation dynamics. These approaches are usually more complex, time-consuming, resource-demanding and require skilled users while, in some cases, still leading to inaccurate results. For this reason, this approach remains an active area of research. Gathering data on erosion damages is generally more feasible through an experimental campaign on a model scale. Nevertheless, establishing a test procedure capable of reliably assessing cavitation erosion power is challenging. The most widely used experimental techniques for erosion risk assessment are based on the guidelines proposed by the International Towing Tank Conference (ITTC 2011). These methods include visual observation of cavitation phenomena, often captured through high-speed video recordings, as well as damage assessment using the soft-paint technique. While these techniques offer valuable qualitative insights, they do not provide a quantitative measure of cavitation aggressiveness. In recent years, various experimental techniques have been developed to address these limitations and provide a more accurate, quantitative assessment of erosive power. Nowithstanding these advancements, several aspects of erosive cavitation remain in need of further investigation.

The situation is slightly different regarding radiated noise. Numerical methods to address this phenomenon are highly resource-intensive and require advanced user skills. Although rather complex, experimental procedures for measuring noise at the model scale and for determining its relative scaling to full-scale applications are quite well established. Even so, these procedures still need to be fully optimized and may be further improved. Moreover, performing experimental tests or CFD simulations for noise prediction during a propeller design phase is not always feasible. In such cases, predictive methods based on empirical calibrations are frequently used. A typical example of these methods is the Empirical Tip Vortex Cavity (ETV) model, proposed in Bosschers 2018. Collecting experimental data that allow strong physical correlations among model parameters would be highly beneficial for such empirical methods. Additionally, such data could support the development of novel and more detailed methods that capture the phenomenon

more comprehensively.

In this framework, collecting experimental data to enable a deeper understanding of cavitation becomes even more important. The work presented in this thesis aims to develop an experimental approach for gathering data on specific cavitation characteristics. Such data include measurements of the size of cavitating structures and their variation over time. Beyond the information contained within the data, these insights would enable the estimation of specific parameters that are challenging to obtain experimentally but are essential for understanding and predicting the effects of cavitation. For instance, by measuring the size variation of a cavitating bubble, it may be possible to estimate the pressure impulse generated by its collapse and assess its aggressiveness or erosive potential. Additionally, these factors heavily influence the prediction of underwater radiated noise. For instance, in many marine applications, noise generated by a cavitating propeller is largely attributed to tip vortex cavitation. This phenomenon is mainly a monopolar noise source which is directly influenced by fluctuations in vortex size over time.

### 1.3 Thesis Layout

In order to make the reading as clear and simple as possible, here is reported a summary of the structure of the thesis and the content of the various chapters. This thesis consists of seven chapters. Chapter 1 presents an general overview of cavitation, emphasizing its significance in marine engineering. In addition a short presentation of the objectives of the present work is provided.

In Chapter 2, the general aspects of cavitation are introduced, highlighting its implication in naval engineering. Furthermore, a detailed description of the primary cavitation phenomena is provided, focusing especially on the physical mechanisms underlying cavitation dynamics.

Chapter 3 provides an overview of the primary effects associated with cavitation phenomena. Specifically, this thesis focuses on two key aspects: cavitation-induced erosion and the radiated underwater noise. The chapter presents the main techniques employed in the study of erosive cavitation and the prediction of cavitation noise. Furthermore, it highlights the opportunities that developing measurement techniques based on high-speed video and computer vision could offer in studying and understanding both phenomena.

Chapter 4 explores the computer vision and image processing techniques employed to analyze cavitation phenomena within the cavitation tunnel. The discussion is structured around the three fundamental phases of any computer vision methodology. Accordingly, the chapter is divided into three sections: selection of the camera model, calibration of the camera, and reconstruction strategies. Each section provides a brief mathematical framework to support the concepts presented. Moreover, the challenges associated with the cavitation tunnel environment and the solutions adopted to overcome these issues are outlined.

Chapter ?? presents the first case study discussed in this thesis, focusing on the application of computer vision techniques to the study of bubble cavitation. This case study was designed to investigate erosive cavitation. In this context, not only the sizes of cavitation bubbles but also their dynamics over time were analyzed. Based on this information, a method was proposed to estimate parameters directly related to the cavitation erosive power, i.e. the magnitude and duration of the pressure pulse generated by bubble collapse.

---

Chapter ?? is dedicated to presenting the second case study. Although still preliminary, this study investigates the relationship between tip vortex cavitation dynamics and the corresponding underwater radiated noise. The study focuses on a model-scale marine propeller tested under various operational and flow conditions. The application of the developed computer vision techniques enabled the reconstruction of cavitating vortices and the analysis of their dynamics over time. Additionally, velocimetry tests were conducted to analyze the flow at the propeller tip, while noise measurements were used to evaluate the radiated noise spectrum. Despite being an early-stage investigation, these analyses have already provided valuable insights into the link between cavitating vortex dynamics and the resulting radiated noise.

Finally, Chapter ?? presents the conclusions of this thesis. This chapter summarizes the strengths and key findings obtained through the proposed techniques. Additionally, it highlights the challenges of applying computer vision to the study of cavitation and discusses potential future developments.

# Chapter 2

## Cavitation Fundamentals

This chapter provides an overview of cavitation, describing the phenomenon's physical aspects and focusing on its relevance to naval engineering. It also includes a brief description of the main types of cavitation present in marine applications. Exploring this aspect of cavitation is essential to underscore the phenomenon's importance, its detrimental aspects, and the main purpose of the thesis, which will be discussed in detail in the following chapter.

### 2.1 General Aspects

Cavitation is a physical phenomenon that occurs when a uniform liquid medium breaks down due to a sudden pressure drop. Generally, the breakdown of the liquid medium can be triggered, forgive less relevant factors, by changes in temperature or pressure. When an increase in temperature causes this breakdown, it is called boiling. Conversely, the phenomenon is known as cavitation when vapour pockets form within the liquid medium due to a pressure drop at a nearly constant temperature (Figure 2.1).

In general, cavitation occurs when the local pressure of the fluid falls below a pressure threshold below which fluid cohesion is not guaranteed. A breakdown in the liquid must occur for vapour pockets to begin forming within a liquid medium. However, the mere reduction of the local fluid pressure below the vapour pressure is not sufficient to drive this process. The Van der Waals isotherm curve (Figure 2.2) shows that the liquid can withstand a certain degree of tensile stress before cavitating (Carlton 2018).

The amount of tension the liquid can tolerate depends on many factors that characterise the fluid from a microscopic point of view. One such factor is the number of particles (or cavitation nuclei) on which pockets of vapour can form and which facilitate the rupture of the liquid medium. However, since the local pressure value of the fluid is still the main factor influencing cavitation, a more macroscopic approach can be adopted, using that parameter as a reference. Figure 2.1 shows the pressure-temperature phase diagram for water. In this diagram, it can be seen that the mechanism that triggers cavitation is a pressure drop. In real applications, this pressure drop is often related to fluid dynamics.

Specifically, depending on the conditions of the liquid in which it occurs, cavitation can usually be divided into three macro-categories. Cavitation can occur in a

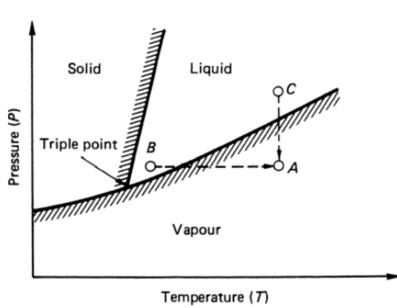


Figure 2.1: Water Phase Diagram (Carlton 2018)

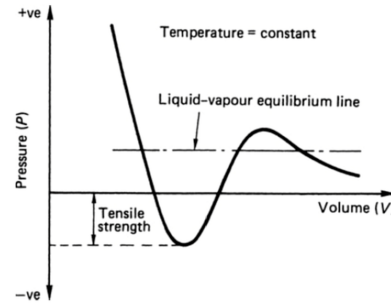


Figure 2.2: Van der Waals' isotherm and definition of tensile strength of liquid (Carlton 2018)

static or quasi-static liquid subject to an oscillating pressure field (if the oscillation amplitude is sufficiently high). This type of cavitation is called acoustic cavitation. Cavitation can also appear after a sudden acceleration of a solid body with sharp edges in a stationary liquid. However, this work is interested only in hydrodynamic cavitation. This concerns fluids moving through narrow passages or around fins, wings, or propeller blades and generally involves high velocity (Carlton 2018, Franc and Michel 2006).

In marine engineering and the maritime industry, cavitation is a phenomenon that often occurs in ship propellers and hull appendages. This phenomenon is usually considered detrimental, resulting in various harmful effects.

Indeed, the dynamics of cavities generate hydrodynamic and acoustic pressure fluctuations, resulting in underwater radiated noise and pressure pulses that induce vibrations on the hull, potentially damaging structures and causing onboard noise. Furthermore, in more severe cases, cavity collapse, vortex action, and cloud cavitation can erode the material of propellers or appendages, leading to a drastic reduction in the object's useful life and a consequent significant increase in maintenance costs.

These phenomena will be discussed in more detail later in this thesis. However, it is important to highlight that cavitation can pose significant challenges to vessel safety, comfort, and operational costs. Despite this, designing propellers that completely avoid cavitation in their operating conditions is not always an effective solution. The design solutions adopted to reduce or delay the onset of cavitation often result in decreased propeller performance.

As a matter of fact, propeller design requires the search for an acceptable trade-off between propeller efficiency and cavitation reduction. While in many cases, an acceptable trade-off can be defined based on simple criteria for reduced cavitation (e.g. verification through the Buril method), for high-performance propellers, larger efforts are needed to optimise propeller performances without incurring cavitation negative effects. Therefore, it is essential to accurately define the threshold beyond which cavitation-related risks can not be accepted. This represents the main motivation of a large part of the research carried out on cavitation in marine applications, including the current thesis. Achieving such knowledge requires deeply investigating the cavitation phenomenon and its effects.

The following section provides a concise overview of the main types of cavitation

affecting marine propellers and hull appendages.

## 2.2 Types of Cavitation

A cavitating flow is a region where fluid appears both in the liquid phase and as vapour. However, in real applications, such as ship propellers, a certain amount of gas is often present in addition to liquid water and vapour. The presence of gas (mainly air) strongly alters cavitating structures' growth and collapse dynamics. For this reason, a cavitating flow is usually treated as a two-phase, three-component phenomenon. Generally, cavitation dynamics are divided into three macro-groups: fixed forms, travelling forms and vibrating forms. However, with regard to marine applications, such as foils or marine propellers, fixed and travelling shapes are of greater interest (Carlton 2018, Knapp et al. 1970).

Generally, cavitation occurring in propellers or hull appendages can be classified as one (or a combination) of the following phenomena: Bubble cavitation, sheet cavitation, cavitating vortices, cloud cavitation. A brief description of each of these phenomena is given below.

### 2.2.1 Bubble Cavitation

To provide a complete description of bubble cavitation, it is first necessary to discuss the behaviour of a single cavitation bubble. Although less relevant to marine engineering practical applications, the dynamics of a single bubble is the phenomenon underlying any more complex type of cavitation. When a cavitation nucleus enters a low-pressure region, it can rapidly expand, transitioning from a microscopic to macroscopic size in a process known as a 'cavitation event' (C.E. Brennen 2014). The bubble continues to grow until external pressure conditions change. As it convects downstream into higher pressure regions, collapse begins, initially with slow contraction followed by a rapid, violent implosion. For instance, Franc and Michel 2006 shows that the entire duration of the collapse phase of a 1 cm radius spherical vapour bubble in water under an external pressure of one bar is approximately one millisecond. At the same time, the duration of the last collapse stage is of the order of one microsecond. Since, from a practical standpoint, the bubble evolves near a solid wall in most of the relevant scenarios, the interaction between the bubble and the body surface has been deeply investigated. As shown in Franc and Michel 2006, the wall's presence alters the bubble's behaviour, causing the bubble to collapse asymmetrically with the formation of a micro-jet. However, this mechanism, which could be modelled as in Plesset and Chapman 1971, differs from the experimental observation in which the flow conveys the bubble. Experimental observations on headforms bodies, presented in Ceccio and C. E. Brennen 1991 show how the viscous boundary layer affects the behaviour of a cavitating bubble. The results of these experiments show a wide difference in the micromechanics of the phenomenon related to the Reynolds number and small variation in the body shape (inducing a laminar separation). Specifically, in the Schiebe headform (Schiebe 1972), when the cavity approaches the collapse region, it takes on a wedge shape wider in the direction transverse to the flow. At the same time, since the bubble occupies flow layers at different velocities, shear effects arise. These effects cause significant spanwise vorticity, making the front side of the bubble twist around itself, generating a cavitating vortex. When the body shape

produces a laminar separation within the region in which the cavitation bubbles occur (e.g. the ITTC headform originally presented in Lindgren 1966), different phenomena are observed. The separation onsets instability in the layer underneath the bubble. This instability appears like a cloudy layer of microscopic bubbles that slides beneath the bubble and is left behind as it evolves. As shown in 2.3, the bubbly layer lasts for a few after the implosion of the main bubble, and two separate collapses occur.

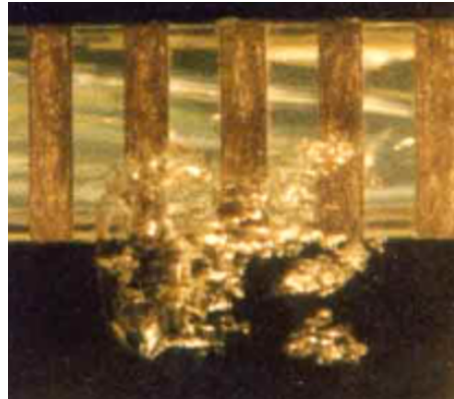
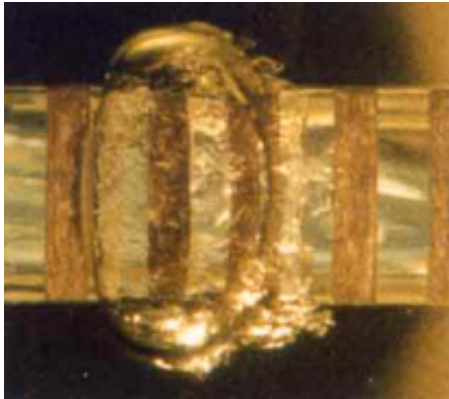
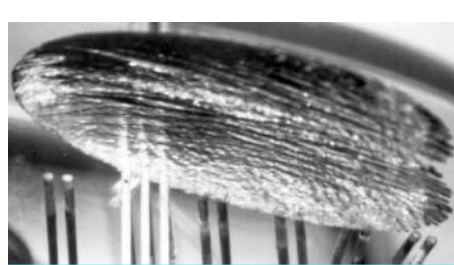


Figure 2.3: Instability of the liquid layer under a traveling cavitation bubble (C.E. Brennen 2014)

During these experiments, occasional bubbles formed local "attached cavitation" as they passed the point of laminar separation. This "attached cavitation" appeared as "tails" on the spanwise sides of the bubble. Again, as long as the main cavity moves downstream, these tails are left behind, resulting in separate collapses (2.4a). The influence of viscous effects on bubble dynamics is further demonstrated by the experiments presented in Chizelle et al. 1994, De Chizelle et al. 1995. These experiments show that as the Reynolds number increases, the phenomena described above develop further and new ones arise. For example, the occurrence frequency of cavitation attached to "tails" increases. In addition, the tails grow in size until they surround the entire bubble, leaving a sort of cavitation patch as the bubble passes (2.4b).



(a) Attached tails formed behind a traveling cavitation bubble C.E. Brennen 2014



(b) Cavitation patch induced by a traveling cavitation bubble C.E. Brennen 2014

In cases of practical interest for marine applications, bubble cavitation often occurs near a solid body that induces a specific pressure field in the fluid. Specifi-

cally, it mainly affects the central portion of hydrofoils operating at a low angle of attack, propeller blades at the root, where the thickness is at its greatest, or the most heavily loaded sections when operating under no-impact conditions, i.e., at a small angle of attack (2.5). In this case, the occurrence of cavitation "events" increases considerably due to various scale effects (including the increased number of Raynolds and the significant increase in the number and size of cavitation nuclei). In real applications, this leads to many bubbles interacting with each other, further modifying their dynamics. Analysing cavitation on hydrofoils or ship propellers, it has been observed that the cavitating bubbles, if in enough number, coalesce into agglomerates characterised by strong instability. By further simulating cavitation, the coalescence of the travelling bubbles forms a single cavitating body. This structure remains stable, sustained by incoming bubbles, and releases cavitating vortices downstream made of microscopic bubbles.

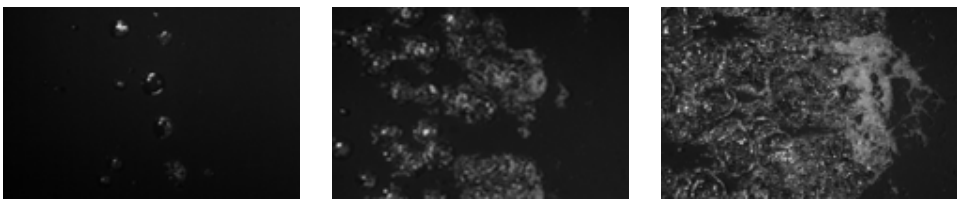


Figure 2.5: Bubble cavitation on a NACA 0015 hydrofoil for different cavitation number conditions

### 2.2.2 Sheet Cavitation

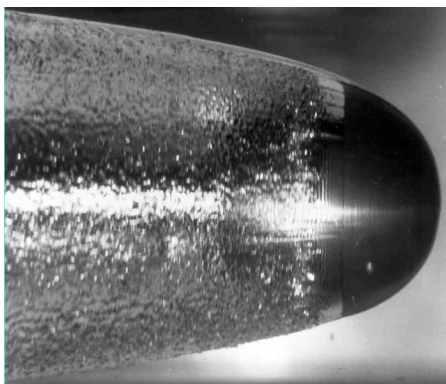
Sheet cavitation, also known as attached cavitation, appears as a single vapour-filled separation zone. This vapour region is generally very stable and remains in approximately the same position. For this reason, it appears to be attached to the surface on which it develops. The appearance of sheet cavitation depends on the conditions under which it is generated. In general, the sheet cavitation surface may appear glossy (especially at model scale) while, in other cases, it may not be transparent and show some instabilities. As already done for bubble cavitation, it may be helpful to refer to some simplified examples to clarify better what mechanisms govern sheet cavitation. Studying bluff bodies, Christopher Brennen 1970 noted that, when further stimulated (e.g. by reducing the cavitation number), the travelling bubble cavitation can show a sudden change, passing to a single vapour-filled wake (Figure 2.6a).

The experiments on bluff bodies showed that sheet cavitation strongly depends on the forebody shape of the tested objects and the flow conditions. Specifically, it was noted that when a sharp edge causes a boundary layer detachment in a laminar flow region, the leading edge of sheet cavitation is well-defined, and the surface is smooth and glassy. For some head forms, the cavitation preserves this glossy aspect almost indefinitely, while for others, the interfacial boundary layer may rapidly pass to a turbulent interfacial layer. The cavitation leading edge may be jagged in other cases, forming quite unstable and bubbly sheet cavitation. In general, sheet cavitation often develops in separate flows, or at least that separation helps its development.

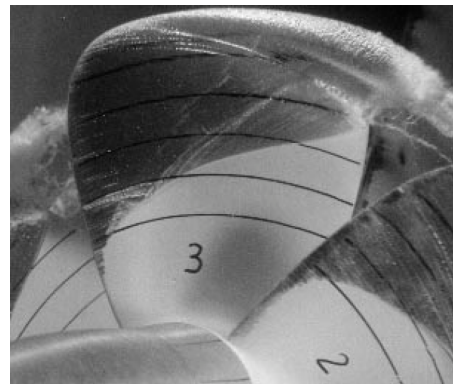
In cases of more practical interest for marine engineering, sheet cavitation can be

found on hydrofoils or marine propeller blades. Specifically, this type of cavitation generally occurs when profiles work at a certain angle of attack. In this case, the pressure distribution on the foil shows a minimum strongly shifted towards the leading edge and a sharp trend. This pressure distribution is characterised by a solid adverse gradient, i.e. an area downstream of the minimum peak where the pressure rises rapidly. The adverse gradient facilitates the separation of the boundary layer and, thus, the development of laminar cavitation. For this reason, sheet cavitation can also be found on the pressure side of profiles. When there is a small suction region on this side of the blade, the adverse gradient is highly steep as the flow passes from a suction region to overpressure in a short space. These observations agree with the results of Kermene [1956](#) that the hydrofoils tested showed bubble cavitation for small angles of attack, while there is sheet cavitation for angles greater than  $10^\circ$  or less than  $-2^\circ$ .

As with headforms, sheet cavitation on foils or propellers can have very different aspects and dynamics. Specifically, it is worth differentiating various cavitation regimes based on the cavitation extent and risks involved. Generally, when sheet cavitation starts to form, it appears as a stable layer above the foil (Figure 2.6b), and the interface between liquid and vapour is easily distinguishable. As it develops, some instabilities arise, and the surface becomes progressively less smooth and bubbly.



(a) Single Fully Developed Vapour Cavity  
(C.E. Brennen [2014](#))



(b) Stable sheet cavitation on the blade of a propeller model (G. Kuiper [1998](#))

Specifically, as cavitation increases, the flow near the cavity closure becomes more and more important. The presence of sheet cavitation causes the boundary layer to detach from the body and a new interfacial boundary layer to form. Since the cavity pressure is near the equilibrium vapour pressure, this interface can be considered a free surface, characterised by a constant pressure. A constant pressure on the free surface requires a smooth attachment between the streamline and the foil. As this is not usually the case, part of the fluid re-enters the cavity and forms a re-entrant jet. In addition, the turbulence level in the interfacial boundary layer increases as it approaches the closure region. For this reason, in real applications, the flow at the cavity closure is always turbulent, leading to a re-entrant jet appearing like a cloudy and turbulent mass.

If the cavitation develops further, it may cover the entire surface of the foil or even extend beyond it. Under these conditions, the flow becomes highly unstable, and the cavitation generally assumes periodic dynamics, whereby a cloud cavita-

tion forms and collapses in an oscillating manner. Furthermore, the flow (especially the re-entrant jet and the collapse of the cloud) releases significant vorticity into the flow, which gives rise to vortices (e.g., horseshoe vortices). The following paragraphs will describe these phenomena in more detail.

### 2.2.3 Cloud Cavitation

The definition of cloud cavitation is even more ambiguous than for other phenomena, however its study is of utmost importance, being cloud cavitation collapse recognised as one of the main causes of cavitation erosion. Cloud cavitation is defined in C.E. Brennen 2014 as the periodical formation of clouds of bubbles, with reference to phenomena such as the periodical shedding of cavitating vortexes or the periodical fluctuations of cavitation occurring on a propeller in behind hull conditions. In Carlton 2018 it is described as a mist or cloud of small bubbles, frequently observed behind large sheet cavitation. In Franc and Michel 2006 a clear definition of cloud cavitation is not given, however cloud cavitation is often mentioned as a consequence of other phenomena, with a specific focus on the case of “cloud instability” which is the periodical shedding of cloud cavitation at the closure of sheet cavities. In addition these Authors identified another phenomenon with common characteristics with cloud cavitation, i.e. shear cavitation. This is the cavitation occurring in the shear layers present in the wake of objects, around submerged jets or at the borders of recirculating regions behind a foil in stall conditions.

As a matter of fact, cloud cavitation consists of a macroscopic, dense assembly of tiny bubbles, usually looking like white clouds in videos, photographs or visual observations, as visible in Figure 2.7. Frequently, cloud cavitation occurs within vortical flows; therefore, it takes the form of cavitating vortexes. The interaction between vortexes and cloud cavitation may take various forms: cloudy structures are often collected by vortexes which become visible being tracked by cavitation, on the other hand vortexes may contribute to the production and subsistence of cloud cavitation.

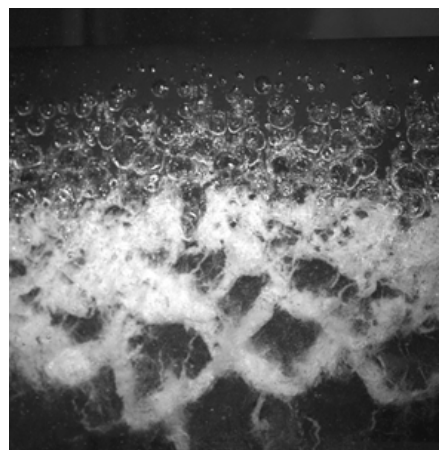
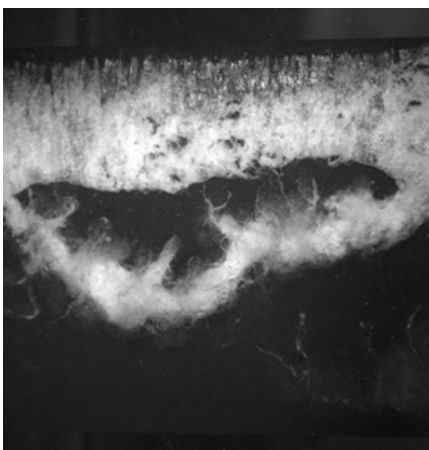


Figure 2.7: Cloud cavitation on a NACA 0015 hydrofoil: production of cloud cavitation downstream of sheet cavitation (left) and downstream of travelling bubble cavitation (right).

Cloud cavitation usually appears as the evolution or deterioration of other cavitation phenomena, such as attached cavitation, bubble cavitation. Its production is mostly associated with the presence of high shear regions in the flow field around the main cavity.

These conditions are typically met at the closure of attached cavitation, where the formation of a re-entrant shed may trigger the periodical break-up of cavitation with the shedding of vertical cloud cavitation. The occurrence of this periodical cloud shedding is highly related to the characteristic of the attached cavity and the resulting re-entrant jet, as point out in Franc and Michel 2006, however some similar cavitation can be observed also at the closure of stable cavities, where large periodical events are not present. As an example two distinct behaviours can be observed at the closure of the sheet cavity on the suction side of a propeller blade shown in Figure 2.8.

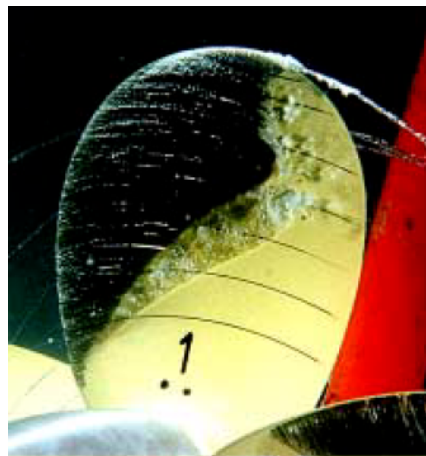


Figure 2.8: Stable sheet cavitation on the suction side of a propeller blade (G. Kuiper 1998).

Actually, cavity closure at inner radii consist of a clear line without significant cloud shedding, while at outer radii many small cloud structures are shed at the closure of the sheet cavity without however the presence of any global cavitation instabilities. In both cases some re-entrant jet is present. At inner radii this jet is clearly present but it does not cause any breakup of the sheet cavity. However a certain amount of bubbles is observed within the jet, which could be considered as some limited cloud cavitation produced by the shear in the jet. In the outer region instead the re-entrant jet is hardly visible while the sheet cavitation continuously breaks locally, shedding small cloudy structures. As a matter of fact only the shed cavitation at outer radii can be rigorously identified as cloud cavitation, however the bubbly flow within the re-entrant jet of a stable cavity presents similar features.

Cloud cavitation can be generated also in other situations, such as the collapse of larger cavities and the successive rebound, if any (Figure 2.9, 2.10).

#### 2.2.4 Vortex Cavitation

Vortex cavitation arises in flows characterized by high vorticity and steep velocity gradients. While irrotational flows present the minimum pressure at the fluid



Figure 2.9: Cloud cavitation produced by vortex bursting on a full scale propeller Carlton 2018.

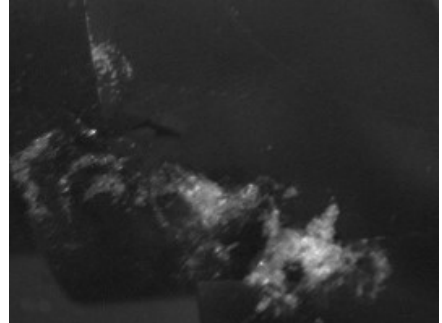
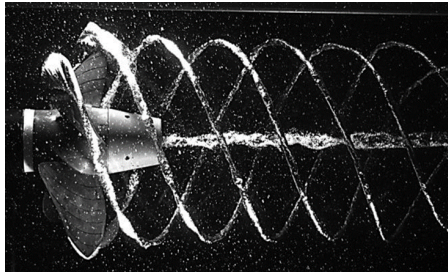


Figure 2.10: Cloudy cavitation structure resulting from the rebound of a collapsing cavity at the root of a propeller blade.

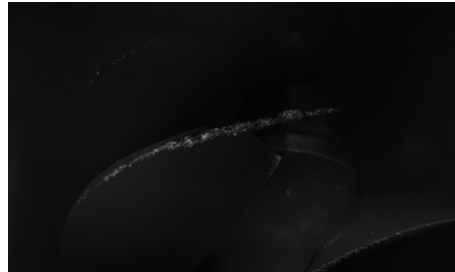
boundary, in high vorticity flows, the suction peak is observed within the core of the vortex structure. When the pressure within this core reaches sufficiently low values, it can fill with vapour and trigger vortex cavitation. The pressure difference between the external flow and the vortex core can be very high. Due to these pressure gradients, in engineering applications (e.g. marine propellers), vortex cavitation onset often precedes other cavitation phenomena. In order to give a clearer idea of vortex cavitation, it is helpful to differentiate types of vortices adopting the classification proposed in Franc and Michel 2006. According to this criterion, coherent and almost steady-state vortices should be distinguished from the vortex structures often observed in shear flows and strongly influenced by turbulence.

Both types are often encountered in marine applications. Coherent vortices often originate near or attached to solid bodies that provide circulation to the vortex. Typical examples of these vortices are the tip vortices often observed in ship propellers or finite aspect ratio hydrofoils. In this case, the onset of the cavitation vortex occurs in a region of intense vorticity, generally some distance from the solid body (Figure ??). By further reducing the value of the pressure in the vortex core (e.g. by increasing the load on the propeller tip), the cavitation grows as it approaches the body until it sticks to it (Carlton 2018, C.E. Brennen 2014). Other examples of coherent vortices can be found in the vortex flows in the draft tube of water turbines or at the hub of ship propellers. This phenomenon, called 'hub vortex', is generated by vortices originating from each blade root of the propeller. These vortices are smaller and not prone to cavitation, but as they are dragged downstream by the shape of the hub, they merge to form a stronger vortex. If this vortex is strong enough to initiate cavitation, a very stable cavitating vortex will result (Figure ??). Finally, leading-edge vortices, which develop on delta wing foils or, in some cases, on marine propellers, also belong to this category. These vortices are generated and sustained by the circulation produced by lifting surfaces and have a stationary character. For this reason, they can certainly be classified as coherent vortices. However, upon closer examination of the formation process, flow separation and shear flows at the leading edge play a contributing role (Figure 2.11b).

Unlike coherent vortices, the vortical structures developed in shear flows do not originate due to circulation produced by lifting surfaces but are generally free.



(a) Tip and hub vortex cavitation observed on a model-scale propeller.

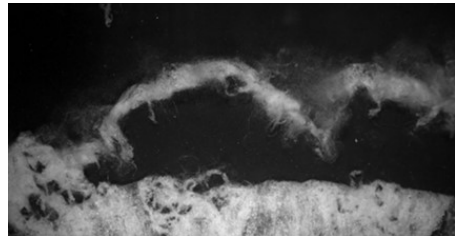


(b) Leading edge vortex cavitation observed on a model-scale propeller.

These vortices are not stationary but propagate into the flow. The absence of a continuous circulation source, combined with their unsteady character, makes them susceptible to viscous dissipation. Consequently, shear vortices typically show a limited duration in time. In practical cases, shear cavitation vortexes often appear downstream of bluff bodies. A typical example is the cavitation associated with the alternating Bénard–Kármán vortices, which develop downstream of wedges or spheres (Figure 2.12a).



(a) Bénard–Kármán Cavitating Vortices in the Separated Wake of a Lifting Flat Plate with a Flap C.E. Brennen 2014.



(b) Horseshoe Vortexes Observed Downstream Cloud Cavitation on a Hydrofoil NACA 0015.

More significant for naval applications are the shear vortices or vapour filaments generated by other types of cavitation. These structures often form downstream fully developed sheet cavitation or cloud cavitation or can be generated by other cavitating vortices. These phenomena include, for instance, horseshoe vortexes, which are often associated with cavitation erosion, or other vortex phenomena already briefly presented in previous sections (Figure 2.12b).

# **Chapter 3**

## **Main effects of cavitation on marine propellers**

This chapter delves into the critical aspects and risk factors associated with previously discussed cavitation phenomena. A specific focus is posed on erosive cavitation and underwater radiated noise caused by cavitation. Although these topics represent only a portion of cavitation-related challenges, they can serve as excellent case studies. Issues such as hull-transmitted vibrations and pressure pulses can somewhat resemble the cases examined in this chapter.

The main goal of this chapter is to present the state of the art in experimental techniques employed in cavitation research. Special attention is given to the most advanced methods, examining their strengths and weaknesses to provide a comprehensive overview. These discussions will clarify the reasoning behind the methodological choices and case studies selected for this work.

### **3.1 Cavitation Erosion**

It has already been mentioned above that under certain conditions, certain cavitation phenomena (e.g. bubble cavitation, unstable laminar cavitation and cloud cavitation) can lead to the erosion of hydrodynamic components. However, it is important to emphasize that the occurrence of potentially erosive phenomena only leads to cavitation in some cases. In contrast, the phenomenon is not intense enough to cause material damage in other scenarios. For this reason, the presence of the phenomena mentioned above can be accepted in many cases, provided that their extent and violence are not excessive. In this context, the prediction of flow aggressiveness is particularly important. This prediction should provide a criterion for defining whether the phenomenon under observation is acceptable or whether it can actually cause damage. The availability of precise and reliable criteria for the acceptability of phenomena provides great advantages in design (e.g. of the ship's propeller) as it helps the search for the optimal compromise between conflicting objectives such as reducing cavitation and maximising efficiency.

For these reasons, several methods for predicting the erosive power of certain cavitation phenomena have been developed over the past years. The following section will present the methods that constitute the state of the art for investigating erosive cavitation.

### 3.1.1 Theory and Modeling Approaches

The cavitation erosive power is closely linked to cavity collapse phenomena near a solid surface. Indeed, The collapse of a bubble results in the generation of extremely high pressures and velocities that apply significant mechanical forces to the material, potentially leading to localized damage. The intensity of the erosive action depends on specific characteristics of the cavitation (e.g. size of the cavitation bubbles, collapse velocity, external pressure, bubble content, focusing of energy during collapse). Consequently, to estimate the erosive aggressiveness of cavitation, it is necessary to obtain an evaluation of some of these quantities or quantities that correlate with them. Measurement of the numerical solution of the phenomenon in its wholeness is impractical, which is why models are widely used to study erosion.

Basically, the models adopted to describe cavitation can be distinguished into two categories corresponding to the two physical phenomena commonly believed to be responsible for erosion (Lecoffre 1999): microjets and shock waves. The intensity or energy associated with these phenomena is then related to specific flow and cavitation characteristics that can be calculated or measured experimentally. In the case of the microjet scheme, an attempt is made to calculate the jet velocity based on the flow characteristics (Peters, Lantermann, et al. 2018). For example, a jet velocity formulation has been proposed (Dular and Coutier-Delgosha 2009; Peters, Sagar, et al. 2015). For approaches based instead on the "shock wave" scheme, the intensity of the erosive action of cavitation is linked to the concept of the bubble's potential energy, which corresponds to the work done by the external pressure during collapse (Hammitt 1963; Pereira et al. 1998; Vogel and Lauterborn 1988), as shown in Equation 3.1:

$$E_C = \Delta P V_C \quad (3.1)$$

Where  $\Delta P$  represents the difference between the external and internal pressure of the bubble, and  $V_C$  is the volume of the bubble. The measurement of the size of cavitation bubbles is one of the main objectives of the present work, so the techniques that can be used for this purpose will be discussed below. However, it should be noted that this measurement can only be carried out for macroscopic cavities and not for microscopic ones (e.g. individual bubbles that form cloud cavitation). This is one of the limitations of the proposed approach as well as of much of the work available in the literature. However, it should be noted that characterising the size of the bubbles forming the cloud would be technically prohibitive for complex applications such as a ship's propeller. In addition, information about the macroscopic structures of cavitation correlates with the dynamics of microscopic structures, thus providing valuable information for describing the cavitation erosive power.

Some attempts can be found in the literature which, by considering the macroscopic structures, tried to obtain various informations required to evaluate both the potential energy of cavitation and, as far as possible, the process of converting this energy into acoustic energy radiated by the shock waves. These kinds of approach is used in most of the numerical erosion models. Notable example of these methods as presented in Köksal et al. 2021; Leclercq et al. 2017 or Usta and Korkut 2019. In these approaches, it is assumed that the instantaneously radiated energy is equal to the potential energy variation provided shown in Equation 3.2

$$\dot{e}_{\text{pot}} = -(p - p_v) \frac{D\alpha}{Dt} - \alpha \frac{Dp}{Dt} \quad (3.2)$$

In this equation,  $\alpha$  defines the vapour fraction (the mixture approach is adopted),  $p_v$  is the vapour pressure and  $\frac{D}{Dt}$  represents the material derivative. In a numerical simulation, the vapour fraction, the pressure, and thus their derivatives, are calculated for each cell and each time-step. Using these values the erosive power of the impacts on the surface is derived by appropriately propagating the pressure pulses.

Although this approach provides valuable insights into erosion mechanisms, it remains constrained by some limitations. One major issue is determining a threshold for erosive intensity beyond which actual damage occurs. Current scientific literature offers limited indication in this framework, but comparisons with experimental data and practical experiences might provide a basis for defining such thresholds. A proposed solution by Usta and Korkut 2019 attempts to address this issue. Nevertheless, its effectiveness is debatable, as it relies on the intensity statistics of the phenomenon under analysis, whereas a threshold would likely benefit from a more universal approach. However its effectiveness is questionable as it is relies on the intensity statistics of the phenomenon under analysis, whereas this kind of threshold should reasonably be based on a more general value criterion.

Further developments of this model were proposed by Melissaris et al. 2020. In this work, the Authors assign specific physical meanings to the two material derivatives present in 3.2: the derivative of the vapour fraction corresponds to the portion of potential energy turned into kinetic energy during the cavity collapse, while the derivative of the pressure corresponds to the portion converted into inertial kinetic energy (e.g. acceleration of the bubble due to the pressure gradient).

From these considerations, the Authors deduce that the share of energy actually involved in the erosive process is just the one linked to the collapse. For this reason, the term related to the material derivative of pressure is neglected. Furthermore, the Authors propose a method for modelling energy conversion from potential to the actual energy radiated by the shock-wave corresponding to the energy involved into the erosive action. This method introduces a kinetic energy field  $\epsilon$  that must fulfil the related transport equation with production terms. This term allows describing not only the energy conversion but also the advection of collapse kinetic energy through the flow, which plays an important role in the concentration of energy, a driving factor of erosive mechanisms.

Other approaches, such as those proposed by Arabnejad et al. 2020 and Schmidt et al. 2008, are based on the assessment of pressure pulses induced to the body surface by acoustic waves (i.e. shock-waves) generated by cavitation collapse. Such approaches obviously require the simulation of compressible flows.

### 3.1.2 Experimental Approaches for Cavitation Erosion

The observations presented thus far offer a brief outline of the most common techniques for estimating cavitation intensity through numerical solutions. The experimental approach proposed in this study relies on similar theoretical foundations but must necessarily account for the different nature of data acquired through experimental methods. Experimental methods allow for a direct examination of the phenomenon and a detailed observation of its dynamics, which cannot be fully captured through numerical models. However, reproducing the precise datasets used

in numerical simulations through experimentation is challenging. The guidelines provided by the ITTC 2011 provide both a reference and a good starting point for analysing the state of the art of current experimental techniques for predicting erosive cavitation. The ITTC procedure is based on a combination of soft-paint coatings and high-speed videos. Soft paint coatings allow for the detection of erosive cavitation, acting as a sensor. By performing endurance tests, cavitation's aggressiveness can be investigated by observing where, how quickly and how much paint is removed. High-speed observations allow to verify the actual presence of potentially erosive phenomena (e.g. collapse, cloud cavitation) and their correspondence with the damage observed on the paintings. Examples of experimental experiences based on this approach can be found in Mantzaris et al. 2015; Pfitsch et al. 2009. To better clarify the objectives and the possible improvements of the ITTC procedure, it is interesting to consider the guidance provided for high-speed video analysis. For this reason, the following is an excerpt from the original document.

“Basic steps to analyse high-speed video recording should focus on:

- Detecting the existence of violent rebounds
- Estimating the violence, the whiteness and the volume of the rebounded cavity. The whiter the rebounding cloud, the more erosive the collapse can be. A fast rebounding cavity is also regarded as potentially erosive.
- Estimating the position of the rebound and its distance from the body surface. The position is important to figure out if possible actions like blade cutting or redesigns to move the collapses outside of the blade can be successful.
- Checking the occurrence of foggy cavitation (a sparse distribution of very small bubbles). It normally can be used as a collapse indicator. Its production is more intense when violent collapse occur.
- Observing the structure of the focusing cavity (glossy, cloudy or mixed). This gives information on the presence of re-entrant jets and contributes to the high risk assessment.
- Estimating the acceleration and the distribution in time of the collapses' motion of the focusing cavity.”

This description provides insights into the quantities to be characterised. In particular, much focus is placed on the presence and intensity of rebounds, as well as the presence of cloud cavitation and macroscopic collapses (focusing cavity). On the other hand, the ITTC description is absolutely vague as to how specific cavitation characteristics should be estimated, such as the "violence" of collapses and rebounds. Another clearly poor aspect concerns the use of the "whiteness" of cavitation as a criterion. In fact, while certainly cloud cavitation and rebounds typically appear very white in the images, it is also true that the degree of whiteness cannot be used as a measure for comparing different cases as it is strictly dependent on the experimental setup, optical access and illumination used.

In this regard, several techniques have been developed over the past few years with the potential to overcome some of these limitations. In Capone et al. 2024, a method based on Laser Doppler Velocimetry (LDV) is presented, apt to quantitatively analyse the size of cavitation developed by a propeller. This method may

allow for the reconstruction of the phase average cavitation volume. However, it does not allow the time-resolved analysis of cavity dynamics. In this regard, several techniques have been developed over the past few years with the potential to overcome some of these limitations. A multi-view line-sensing method was proposed in Shiraishi et al. 2024 to reconstruct the shape of cavitation on propeller blades. This approach is very interesting and offers an accurate measurement of cavitation volume. However, like the previous one, it cannot be used to observe the dynamics of a single event over time. Other approaches, such as that proposed by Vijayan and Pradeep Kumar 2023, enable the investigation of cavitation within the time domain, allowing for the analysis of modal frequencies. However, addressing cavitation erosion by applying these methods, based on shadowgraphy and high-speed imaging, is generally unfeasible (especially in cases of engineering interest, such as a ship propeller).

Among the explored alternatives, techniques based on computer vision algorithms appear particularly promising. These techniques offer the potential for quantitative, time-resolved cavitation measurements. However, their implementation involves several technical challenges, including optical access to the target region, the quality of captured images, and the complexity of identifying and segmenting the cavities of interest. Nevertheless, the scientific literature provides some examples of applications in the cavitation tunnel environment (Franzosi et al. 2023, Ebert and Damaschke 2019).

It is particularly worth mentioning studies by Pereira et al. 1998 and Savio et al. 2011. A volumetric visualisation and reconstruction technique by combining stereometry and tomography to quantify the volume of cavities on a NACA 65012 is proposed in Pereira et al. 1998. This method uses a laser measurement technique to estimate the principal size of the cavities. Then, using a stereometry technique known as shape by silhouette, a more precise estimation of the volume for some cavities is obtained, proving a strong correlation between it and the estimate obtained with the laser.

The work of Pereira et al. 1998 has been partially adopted by Savio et al. 2011. In this study, the Authors use various computer vision techniques to study cavitation. The work of Pereira et al. 1998 has been partially adopted by Savio et al. 2011. In this study, the Authors use various computer vision techniques to study cavitation. Specifically, an active triangulation technique is developed to accurately measure the extent and thickness of sheet cavitation. A shape-by-silhouette technique (similar to Pereira et al. 1998) is proposed for the study of tip vortex cavitation.

Although these methods are extremely interesting and offer valuable information regarding cavitation, they are limited in studying cavitation mechanisms and dynamics. Part of the present work's objective is to develop these techniques further in order to address not only the cavity's size but also its evolution over time.

This approach would allow for combined observation of data that capture the potential energy of cavitation (such as the size of macroscopic structures) with dynamic quantities. This kind of data, including the velocity of the bubble collapse and the number or the extension of the rebound, provides valuable information on how this energy is released.

Besides providing a deeper understanding of the phenomenon, such data could help overcome some of the limitations of the ITTC procedures. Indeed, measurements of the cavity size and its variation over time could be used to define more

precise, quantitative and general criteria for predicting the aggressiveness of erosive cavitation.

## 3.2 Cavitation Underwater Radiated Noise

The onboard machines and propellers are the main sources of underwater radiated noise (URN) from ships. However, numerous studies (Ross 2013) have shown that, when cavitating, the propeller is by far the primary source of noise. When cavitation phenomena are present, the URN rises significantly. Specifically, the major cavitation contribution to URN arises from the sheet and tip vortex cavitation. The volume variation and especially the volume acceleration during the collapse phase of the sheet cavitation is recognized as a powerful source of underwater noise. While the tip vortex and the pressure pulsations associated with it are generally linked with a broadband hump (Lloyd et al. 2020)

Radiated noise from ships is an important design constraint when designing a ship's propeller. In fact, in both the civil and military fields, there are good reasons to reduce radiated underwater noise as much as possible. In the civil field, radiated noise is a severe environmental problem. Several studies (Rojano-Doñate et al. 2023) have proven that, especially in the busiest areas, the acoustic pollution produced by ships negatively affects the marine environment. For this reason, although there are no mandatory laws, several international organisations are promoting guidelines and best practices to reduce radiated noise (International Maritime Organization (IMO) 2023). High levels of radiated noise are often linked to noise and vibrations transmitted to the hull. This phenomenon is a major issue, especially for comfort on board passenger ships, and can make working conditions unpleasant for the crew. In some cases, continuous exposure to high noise levels can have significant repercussions on human health, compromising the health of people on board. In the military field, the noise radiated by ships is of considerable strategic importance. Indeed, the acoustical signatures of a ship can compromise its ability to operate undetected, which constitutes a significant security problem.

For these reasons, predicting the underwater noise emitted by a cavitating propeller is of great interest to ship designers. Many efforts have been made in recent years to achieve this goal.

### 3.2.1 Theory and Modeling Approaches

From a physical point of view, the noise production of a ship's propeller (as of any other source) can be attributed to three main mechanisms. Acoustic sources are usually classified into monopolar, dipolar and quadrupolar sources. These sources describe how sound is generated and radiated into the environment. Each source type has specific characteristics and can be associated with different physical phenomena (Russell et al. 1999).

Monopolar sources are typically associated with phenomena involving a medium's volumetric expansion and contraction. In marine applications, such volume variations frequently arise in the dynamics of cavitating structures. For this reason, monopole sources are widely considered the primary contributors to cavitation noise. A typical monopolar source is the collapse of cavitating structures. When a cavitation bubble collapses, a rapid volume change occurs, which is associated with a strong acoustic impulse that propagates isotropically in the water. How-

ever, it is essential to highlight that the collapse of cavity structures is not the sole mechanism responsible for producing monopolar noise in cavitation phenomena. Even minor volumetric variations of cavitating structures can act as monopole sources. Consequently, predicting noise radiation in water necessitates observing the dynamics of all cavitating structures. For instance, the tip vortex is among the cavitation forms most associated with underwater noise radiation. While this phenomenon does not typically involve violent collapses, except under specific conditions, the volume variations and fluctuations during the vortex's evolution are widely recognised as a significant source of acoustic emissions (Bosschers 2018).

Two monopoles of equal intensity, opposite phase, and separated by a small distance form a dipole source. In this case, when one monopole “expires,” the other “inspires,” and the surrounding fluid oscillates back and forth between the sources. Dipole sources are often associated with pressure forces acting on solid surfaces in interaction with the fluid. A characteristic example of dipole sources is the forces generated by the propeller blades during rotation. Periodic variations in lift and drag induce pressure oscillations that propagate as sound waves. The acoustic radiation efficiency of dipole sources is lower than that of monopole sources, as the waves generated by the two poles partially cancel each other in specific directions. Quadrupole sources arise from more complex force distributions, such as those generated by stress gradients or turbulence. These sources are typical of turbulent flows. Quadrupole sources are even less efficient than dipole sources, as the radiated acoustic power decreases rapidly with distance.

In scientific literature, various theoretical models can be found that describe underwater noise propagation. Among these, the Ffowcs Williams and Hawkings (FWH) equations (Williams and Hawkings 1969) are by far the most widely used (Eqn: 3.3). The FWH equations are derived directly from the Navier-Stokes equations, which govern fluid motion, and represent a generalization of Lighthill's classical wave equation (Lighthill 1952), providing a robust mathematical framework for describing acoustic radiation in water.

$$\square^2 p' = \frac{\partial}{\partial t} [\rho_0 v_n \delta(f)] - \frac{\partial}{\partial x_i} [p n_i \delta(f)] + \frac{\partial^2}{\partial x_i \partial x_j} [H(f) T_{ij}] \quad (3.3)$$

In this equation, the left-hand term  $\square^2 p'$  represents the d'Alembert operator ( $\square^2$ ) applied to the pressure fluctuation ( $p' = c^2 \rho' = c^2 (\rho - \rho_0)$ ) and describes the propagation of waves in the medium. Three distinct contributions are present on the right-hand side, each of which can be associated with a specific acoustic source within the system. The first term,  $\frac{\partial}{\partial t} [\rho_0 v_n \delta(f)]$ , is linked to the normal velocity  $v_n$  at the surface and represents the sound sources dependent on the motion of the surface. This term corresponds to a volumetric variation commonly associated with monopole sources. The second term,  $-\frac{\partial}{\partial x_i} [p n_i \delta(f)]$ , describes the contribution of the pressure gradient on the surface. This term can be associated with dipole sources. The third term,  $\frac{\partial^2}{\partial x_i \partial x_j} [H(f) T_{ij}]$ , is expressed in terms of Lighthill's stress tensor ( $T_{ij}$ ) and the Heaviside function ( $H(f)$ ). This contribution arises from internal stresses within the fluid, such as those due to turbulence, and is, therefore, related to quadrupole sources.

Given their comprehensiveness, the FWH equations are a powerful numerical noise prediction tool e trovano largo uso negli approcci numerici. Several computational fluid dynamics (CFD) studies, such as Testa et al. 2018, have demonstrated that approaches based on the FWH equations yield significantly more accurate

results than traditional methods relying on Bernoulli's theorem. Nevertheless, applying the Ffowcs Williams Hawkings equations to complex case studies, such as the analysis of cavitating flows, is quite complex.

Solving noise production and propagation simultaneously in a single calculation is usually too complex. For this reason, the acoustic sources and noise propagation are studied separately in most analyses. In these analyses, acoustic sources are usually characterised through computational fluid dynamics (CFD) tools, while post-processing calculations determine noise propagation through acoustic analogies, such as the FWH equations. Due to the complexity of the problem, such analyses can be highly computationally demanding. For this reason, simplifying solutions are often adopted. One of the most common simplifications is the so-called "porous surface". Following this approach, the acoustic effects of noise sources can be implicitly evaluated through surface integrals without the need to perform volumetric integration. While this simplification introduces some approximations and challenges, it significantly reduces the complexity of the problem.

### 3.2.2 Practical Noise Prediction

It is even more challenging to provide a reliable prediction of the underwater noise radiated by a cavitating propeller at the design stage.

As previously discussed, it is possible to accurately reproduce noise generation and propagation mechanisms through sophisticated numerical simulations and acoustic analogies. However, this does not imply that the issue of noise prediction is fully resolved. These methods are intrinsically complex and demand significant computational time and resources. In addition their effectiveness requires the complete and accurate solution of turbulent scales and cavitation dynamics, which can be prohibitive with commonly used cavitation models and mesh sizes. Consequently these methods are impractical for application during the early stages of the design process, when multiple geometries and operating conditions need to be evaluated. Their use is mostly limited to research and in some cases to the verification of the final propeller design.

A similar comment can be extended to experimental tests conducted on model scales. Although experimental testing remains the most reliable and accurate method for noise prediction, its application during the early stages of design is not economically feasible.

For this reason, more straightforward and cost-effective approaches have been developed over time to provide noise estimates with acceptable accuracy while minimizing both costs and time requirements. The scientific literature offers various examples of these methods that can be grouped into two main categories: semi-empirical and data-driven. Both semi-empirical and data-driven methods extensively rely on experimental data to establish robust correlations between propeller geometries, operating conditions, and the spectrum of radiated noise. However, the utilization of experimental data differs significantly between the two approaches: Semi-empirical methods incorporate data to refine and validate physics-based models. Data-driven methods exploit knowledge of phenomena from experimental datasets to train predictive algorithms.

Semi-empirical methods refer to theoretical formulations that describe a specific phenomenon of interest. Simplifying assumptions are often applied to these formulations, making the equations resolvable without requiring sophisticated computational tools. The resulting simplified models are calibrated using experimental

data to ensure their applicability to real-world problems. Among the most commonly employed methods for predicting noise radiated by a cavitating propeller are those described in Bosschers 2018 and Brown 1999.

The Empirical Tip Vortex (ETV) model presented in Bosschers 2018 enables the calculation of the frequency ( $f_c$ ) and the radiated noise level ( $RNL_c$ ) of the low-to-medium frequency hump typically associated with the presence of tip vortex cavitation. Furthermore, based on these parameters, the ETV model provides an estimate of the radiated noise spectrum. On the other hand, the model proposed by Brown 1999 is used to predict the contribution of sheet cavitation to the noise spectrum. This contribution is generally observed at high frequencies within a band ranging from 10 to 80 kHz. In this framework, developing a method apt to provide accurate measurements of both the extent and dynamics of cavitating structures represents an interesting opportunity for enhancing the understanding and prediction of radiated noise. Indeed, these methods typically rely on some simplified estimate of the extent of the cavitating phenomenon of interest.

For instance, in the formulations underlying the ETV model, as presented in Equations 3.4 and 3.5, the term  $r_c$  represents the radius of the cavitating vortex.

$$\frac{f_c}{nZ} = c_1 \frac{1}{r_c} \sqrt{\frac{\sigma_{\text{tip}}}{Z}} + c_2, \quad (3.4)$$

$$RNL_c = a_p + 20 \log_{10} \left( \left( \frac{r_c}{D} \right)^k \sqrt{Z} \right), \quad (3.5)$$

The method is based on the assumption that the main noise generation mechanism of tip vortex cavitation is the vortex pulsation at its natural frequency, which is responsible of the typical vortex hump in the spectrum. Accordingly, correlations exist between the vortex radius, its pulsation frequency and the resulting noise levels.

According to the method, the vortex cavitating radius is obtained from the velocity field around the vortex, which is, in turn, described by a 2D vortex model. Among vortex models available in the literature, the model of Proctor et al. 2010 allows obtaining a good agreement with experimental data, while the model of Lamb 1932 provides less accurate results. The use of vortex models requires knowledge of the vortex strength as an input parameter. This can be obtained by computations with a Boundary Element Method, or it can be assumed to be roughly proportional to the propeller loading by means of a tip loading coefficient Bosschers 2018. In all cases, the effects of variable vortex strength during blade revolutions, as well as general cavitation dynamics, are not explicitly included in the theoretical formulations on which the method is based. In addition, the validation of the cavitation vortex radius estimates obtained from the vortex models was based on the experimental data collected in Pennings et al. 2015 and Gert Kuiper 1981. However, these data sets do not include measurements of the vortex radius variation as the blade angle varies along the propeller's rotation.

In this thesis, the dynamics of the tip vortex is reconstructed using a method based on computer vision techniques. The availability of tip vortex volume and its dynamics for a range of propeller operational conditions and for various wake fields will allow analysis in detail of the strength and limits of the state-of-the-art vortex models, also providing the basis for the improvement of these models. Among the others, the dominating noise generation mechanism will be investigated, trying to assess under what conditions the vortex pulsation is the main generation process

and when, instead, the radiated noise is mostly produced by the volume variation induced by variable blade loading. In addition, the simultaneous measurement of vortex size and radiated noise will allow further investigation of the correlations between radiated noise spectra and vortex dynamics for a realistic configuration, i.e. a propeller with variable inflow conditions.

### 3.3 Summary

This thesis presents computer vision techniques adapted to work effectively in the cavitation tunnel environment. The main purpose of these techniques is to accurately measure the size of the observed phenomena and study their dynamics over time. The developed methods were applied to two case studies. The first, described in Chapter ??, focuses on bubble cavitation, aiming to analyze bubble collapse dynamics and linked erosion mechanisms. The second, discussed in Chapter ??, addresses the noise generated by cavitation, with particular attention to the dynamics of tip vortex cavitation. These techniques could be extended in the future to study other types of cavitation and to deepen the understanding of additional detrimental effects associated with it.

# Chapter 4

# Computer Vision in Cavitation Tunnel Environment

This chapter delves into the primary computer vision and image processing techniques employed in this thesis to analyze cavitation phenomena observed in the cavitation tunnel. The main goal is to provide a structured overview of the mathematical and algorithmic tools utilized, emphasizing the challenges encountered in their application within a complex experimental environment and the solutions devised to address them. This chapter will be divided into three main sections to make the discussion as clear as possible. The first section will describe the mathematical camera model and the reasons behind its choice. The second section focuses on camera calibration techniques to define a robust relationship between the physical world and the information in the images. Finally, the third and last section will discuss the computer vision techniques used to extract data from high-speed video and obtain measurements of cavity phenomena.

## 4.1 Camera Model

The first step in applying any computer vision technique is selecting the mathematical model to describe the cameras. The literature offers various models tailored to the camera type and the specific application.

In this particular case, it is necessary to adopt a model capable of addressing the air plexiglass water interface characteristic of the cavitation tunnel. Due to the dimensions of the cavitation tunnel at the University of Genoa (described in Appendix ??), placing cameras directly in the water is unfeasible. While placing cameras out of water ensures completely non-intrusive measurements, it requires solving the refraction problem occurring at the interfaces, as illustrated in Figure 4.1.

The work presented in Sedlazeck and Koch 2012 provides a basis for addressing the issue of refraction in the context of cavitation tunnels. This study examines three types of cameras commonly employed in applications similar to those of interest to identify the strengths and weaknesses of each. The first camera model

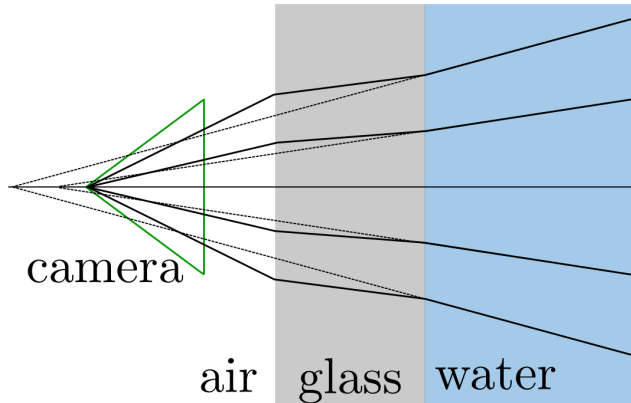


Figure 4.1: Refraction at air-plexiglass-water interface (Sedlazeck and Koch 2012).

considered is the perspective pinhole camera model (single viewpoint model, SVP), characterized by an effective focal length and distortion parameters designed to compensate for the errors introduced by refraction at the camera housing. The second model analyzed belongs to the category of ray-based camera models. These approaches rely on tracing perspective rays and are characterized by a huge number of degrees of freedom. For this reason, as noted in the article, achieving accurate camera calibration in the context of interest is challenging or even unfeasible. Lastly, the last camera model discussed represents an evolution of the pinhole camera model. This approach incorporates a physical description of the interfaces, explicitly calculating the effects of refraction. Although this method shows great potential, the standard pinhole model was preferred in this study. The application of physically-based interface models remains relatively scarce in the literature, and developing a robust calibration procedure that includes the parameters necessary to account for refraction effects is particularly complex.

Conversely, with appropriate adaptations, the pinhole model provides accurate results and is widely used in the literature for similar applications. This model offers several significant advantages. Despite its mathematical simplicity, the pinhole model accurately describes perspective projection. This simplicity makes it user-friendly and allows for considerable adaptability to diverse scenarios. Furthermore, as demonstrated later in this chapter, achieving satisfactory performance is feasible by applying specific precautions. Finally, the simplicity of the pinhole model renders it highly efficient from a computational perspective.

### 4.1.1 Pinhole Camera Model

The Pinhole model is one of the simplest mathematical formulations used to describe a camera's functioning. Despite its simplicity, the model accurately represents basic optical principles, making it a robust and versatile solution for a wide range of applications. The Pinhole model describes the process of perspective projection by modelling the camera as an optical device with an infinitely small aperture (the pinhole) and no lenses (Figure 4.2). Its operational principle is straightforward yet effective: all rays of light passing through the pinhole converge to specific points on the image plane. The aperture acts as a projection centre,

mapping the three-dimensional (3D) world onto a two-dimensional (2D) plane.

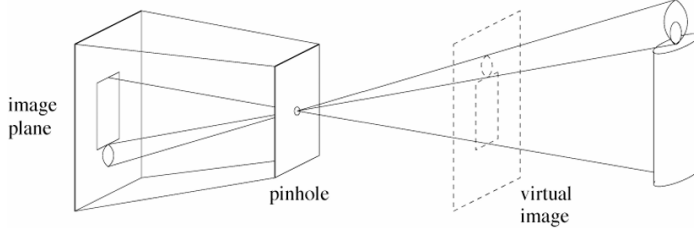


Figure 4.2: Pinhole Camera Model

$$u = f \frac{X}{Z}, \quad v = f \frac{Y}{Z}. \quad (4.1)$$

This transformation, graphically represented in 4.3, is fully non-linear. Managing such transformations in Cartesian coordinates would be extremely complex. For this reason, homogeneous coordinates are introduced.

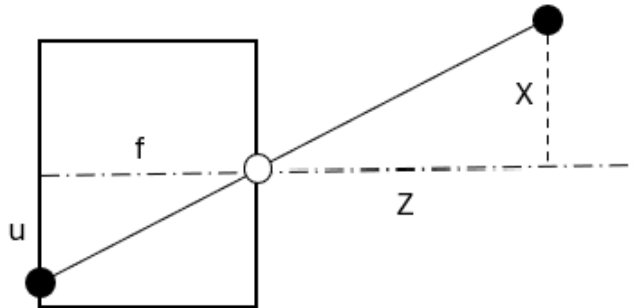


Figure 4.3: Pinhole perspective projection mechanism.

#### 4.1.1.1 Omogeneous Coordinates

Homogeneous coordinates represent an extension of the Cartesian coordinate system by introducing an auxiliary dimension. In three-dimensional space, a point  $P = [X_c, Y_c, Z_c]^T$  is represented in homogeneous coordinates as  $P = [X_o, Y_o, Z_o, w]^T$ , where  $w \neq 0$  is an arbitrary scalar. Similarly, a two-dimensional point  $p = [u_c, v_c]^T$  is extended and represented as  $p = [u_o, v_o, w]^T$ . The relationship between homogeneous and Cartesian coordinates is expressed by Equation 4.2.

$$X_c = \frac{X_o}{w}, \quad Y_c = \frac{Y_o}{w}, \quad Z_c = \frac{Z_o}{w},. \quad (4.2)$$

Where, the superscript  $c$  is used to denote Cartesian coordinates, while the superscript  $o$  refers to homogeneous coordinates. Typically,  $w = 1$  is set by convention to normalize the homogeneous coordinates. This coordinate system offers two

main advantages. The first is the handling of points at infinity. By setting  $w = 0$ , homogeneous coordinates allow for an effective representation of points at infinity. However, the most significant advantage lies in the linearization of projective transformations. In Cartesian coordinates, perspective projection is characterized by a ratio, making it a nonlinear transformation. Conversely, in the space of homogeneous coordinates, it can be expressed as a simple matrix product (Equation 4.3).

$$\begin{pmatrix} u \\ v \\ 1 \end{pmatrix} \sim \begin{pmatrix} f & 0 & 0 & 0 \\ 0 & f & 0 & 0 \\ 0 & 0 & 1 & 0 \end{pmatrix} \begin{pmatrix} X \\ Y \\ Z \\ 1 \end{pmatrix} \quad (4.3)$$

This transformation rules the perspective projection underlying the pinhole camera model. However, it represents only a simplified version of the camera model.

#### 4.1.1.2 General Camera Model

The model presented above must be generalized by considering several factors to describe the operation of a camera in a real-world application.

Firstly, the model is expressed in physical units. The coordinates of the physical points  $[X, Y, Z]$ , the image points  $[u, v]$  and the focal length  $f$  are given in millimetres (or meters). However, in practice, only the focal length and physical points are typically expressed in these units, while image points are measured in pixels. To convert millimetres to pixels, it is possible to introduce two scaling factors,  $s_x$  e  $s_y$ . This allows Equation 4.3 to be reformulated as shown in Equation 4.4.

$$\begin{pmatrix} u \\ v \\ 1 \end{pmatrix} \sim \begin{pmatrix} s_x f & 0 & 0 & 0 \\ 0 & s_y f & 0 & 0 \\ 0 & 0 & 1 & 0 \end{pmatrix} \begin{pmatrix} X \\ Y \\ Z \\ 1 \end{pmatrix} \quad (4.4)$$

In most cases, pixel shapes are square. This implies that  $s_x = s_y$  and consequently  $f_x = s_x f = s_y f = f_y = f$ . Furthermore, the model assumes that the origin of the image coordinate system (in pixels) is located along the camera's optical axis ( $Z$ ). However, this assumption is generally not valid in practical cases, as pixel coordinates are typically measured starting from the image's top-left corner. This requires adding a translation to the transformation defined so far, resulting in the form shown in Equation 4.5.

$$\begin{pmatrix} u \\ v \\ 1 \end{pmatrix} \sim \begin{pmatrix} s_x f & 0 & c_x & 0 \\ 0 & s_y f & c_y & 0 \\ 0 & 0 & 1 & 0 \end{pmatrix} \begin{pmatrix} X \\ Y \\ Z \\ 1 \end{pmatrix} \quad (4.5)$$

In which  $c_x$  and  $c_y$  define the position of the point where the optical axis intersects the image plane. This point is referred to as the principal point.

Finally, in the most general cases, the model introduces an additional parameter,  $\alpha$ , to account for the possibility that the optical axis is not perfectly orthogonal to the image plane. This way, the intrinsic camera model described by Equation

(4.6) is obtained. However, in most cases, the image plane and the optical axis are orthogonal, leading to  $\alpha = 0$ .

$$\begin{pmatrix} u \\ v \\ 1 \end{pmatrix} \sim \begin{pmatrix} s_x f & \alpha & c_x & 0 \\ 0 & s_y f & c_y & 0 \\ 0 & 0 & 1 & 0 \end{pmatrix} \begin{pmatrix} X \\ Y \\ Z \\ 1 \end{pmatrix} = PPM \begin{pmatrix} X \\ Y \\ Z \\ 1 \end{pmatrix} \quad (4.6)$$

In which  $PPM$  is called the perspective projection matrix.

The Projection Perspective Matrix (PPM) reported in Equation 4.6 can be represented as the product of two matrices the matrix of intrinsic parameters  $K$  (commonly referred to as the camera matrix) and the matrix  $[I|0]$  that encodes the essence of the prespective transformation without any parameters. With this distinction, the perspective projection matrix defined in Equation 4.6 can be reformulated as shown in Equation 4.7.

$$PPM = \begin{pmatrix} s_x f & \alpha & c_x \\ 0 & s_y f & c_y \\ 0 & 0 & 1 \end{pmatrix} \begin{pmatrix} 1 & 0 & 0 & 0 \\ 0 & 1 & 0 & 0 \\ 0 & 0 & 1 & 0 \end{pmatrix} = K \begin{pmatrix} 1 & 0 & 0 & 0 \\ 0 & 1 & 0 & 0 \\ 0 & 0 & 1 & 0 \end{pmatrix} \quad (4.7)$$

Even if the Equation 4.6 allows for a general and complete description of the perspective projections, it assumes that points in 3D space can be represented in coordinates relative to the camera's frame of reference (in which  $Z$  is the optical axis). This would make the camera calibration procedure extremely complex (which will be discussed in Section 4.2) or even unfeasible. For this reason, it is preferred to describe the pinhole model using three reference systems (Figure 4.4).

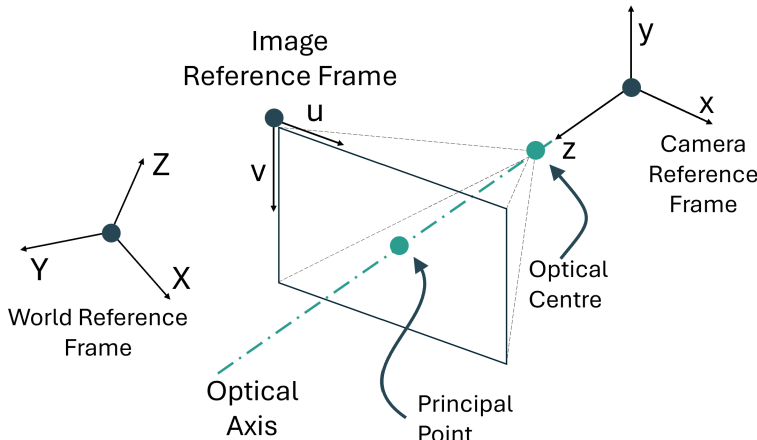


Figure 4.4: Characteristic References Frames in the Pinhole Camera Model

In the discussion above, the relationship between the "camera reference system" (in millimetres) and the "image reference system" (in pixels) was already described (Equation 4.6). In addition, a third reference system is introduced, often called the "world reference system", in which points are expressed in physical space (also in millimetres). This reference system has an arbitrary origin and orientation and is simply an auxiliary system for describing perspective projections and camera

calibration. Assuming that the camera reference system is rotated and translated relative to the world reference system, a rotation matrix  $R$  and a translation vector  $T$  can be introduced to satisfy Equation 4.8.

$$M_c = \begin{pmatrix} R & T \\ 0 & 1 \end{pmatrix} M_w = \begin{pmatrix} r_{11} & r_{12} & r_{13} & t_x \\ r_{21} & r_{22} & r_{23} & t_y \\ r_{31} & r_{32} & r_{33} & t_z \\ 0 & 0 & 0 & 1 \end{pmatrix} M_w \quad (4.8)$$

Where the subscript  $c$  indicates the coordinates expressed in the camera reference frame, while  $w$  refers to the coordinates in the world reference frame. The matrix that relates the camera system to the world system is the extrinsic parameter matrix. It depends on the scene that the camera observes because it takes different values depending on where the origin of the world system is placed. By introducing this last step, it is possible to rewrite Equation 4.6 in the form presented in Equation 4.9.

$$\begin{pmatrix} u \\ v \\ 1 \end{pmatrix} \sim K \begin{pmatrix} I & | & 0 \end{pmatrix} \begin{pmatrix} R & T \\ 0 & 1 \end{pmatrix} \begin{pmatrix} X \\ Y \\ Z \\ 1 \end{pmatrix} \quad (4.9)$$

Unlike what occurs in Equation 4.6, the terms  $[X, Y, Z, 1]$  do not represent the coordinates in the camera system but those in the world coordinate system. This relationship constitutes the perspective projection at the base of the pinhole camera model. The terms in Equation 4.9 can be distinguished into intrinsic and extrinsic parameters. As already mentioned, the matrix  $K$  contains the intrinsic parameters. These terms are characteristic of the camera as long as it works in a homogeneous medium and the lenses remain unchanged. On the other hand, terms in matrix  $R$  and vector  $T$  are the extrinsic parameters fully dependent on the scene observed by the camera.

By examining Equation 4.9, it is possible to count the number of parameters necessary to fully define the model. The intrinsic parameters are five: two focal lengths, two coordinates for the principal point, and the factor  $\alpha$  (often neglected). The latter is typically ignored, meaning the intrinsic parameters to be determined are usually four. The extrinsic parameters include six values: the three angles required to define the rotation matrix  $R$  and the three translation coordinates in the vector  $T$ . In total, ten coefficients must be defined.

Finally, it is important to focus on the assumptions underlying the model. Although previously mentioned, these assumptions should be explicitly addressed to clarify the related issues and solutions adopted. First, neglecting the  $\alpha$  term assumes that the image plane is perfectly perpendicular to the optical axis and that the camera is rigid, without changes in focal length during image acquisition. This assumption is generally valid for high-quality cameras. It is also assumed that the pinhole is infinitesimally small to avoid blurring effects, which implies a trade-off between image brightness and sharpness. Although this assumption is not strictly true, it does not pose significant problems for optical measurements. Lastly, the model assumes that light rays travel in straight lines and that the lenses do not introduce optical distortions or aberrations. Both of these assumptions are entirely false, and they must be properly managed, particularly in non-conventional environments (such as the cavitation tunnel).

### 4.1.2 Distortion Models

The optical system that constitutes a camera can be characterized by a wide range of imperfections that induce image distortions. These imperfections are typically due to the lenses, which are not accounted for by the pinhole model. Ignoring these distortions could result in significant errors, compromising the accuracy of measurements. In general, the effect of distortion can be expressed by the relationships shown in Equation 4.10.

$$u' = u + \delta_u(u, v), \quad v' = v + \delta_v(u, v) \quad (4.10)$$

Where the prime symbol ' denotes the distorted coordinates, while the coordinates without the prime symbol refer to the coordinates in the distortion-free image.

The following section will discuss the standard types of distortions caused by lenses and the commonly adopted models used in the literature to represent and mitigate these distortions (Weng et al. 1992).

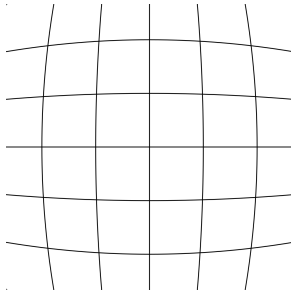
#### 4.1.2.1 Radial Distortion

Radial distortion occurs when light entering the lens undergoes a distortion that increases with distance from the centre of the field of view. This distortion leads to images that are distorted radially with respect to the centre of the camera. The primary cause of radial distortion is often the imperfect curvature of the camera's lenses. In practice, three main types of radial distortion can be distinguished.

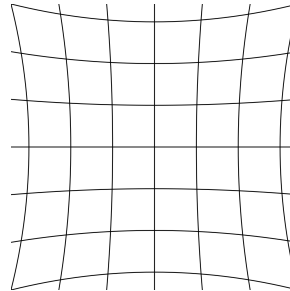
- Barrel Distortion: A negative radial displacement is referred to as barrel distortion (Figure 4.5a). Barrel distortion causes an increase in the distance of outer points. The apparent effect is an image that appears to be mapped around a sphere (or barrel).
- Pincushion Distortion: A positive radial displacement is defined as pincushion distortion. This type of distortion causes the outward dispersion of peripheral points (Figure 4.5b). The effect of pincushion distortion is that lines not passing through the centre of the image appear bent inward toward the centre of the image (resembling a pincushion).
- Moustache Distortion: Moustache distortion can be considered a combination of the previously mentioned distortions (Figure 4.5c). Moustache distortion begins as barrel distortion near the centre of the image and gradually transitions into pincushion distortion toward the periphery. This progression causes horizontal lines in the upper half of the frame to resemble handlebar moustaches.

Radial distortion can mathematically be described by a function that alters the coordinates of points in the image based on their distance from the centre of the lens (which is typically assumed to coincide with the principal point of the camera). Under this assumption, the correction of radial distortion can be achieved through the use of polynomials that model the distortion, as shown in Equation 4.11.

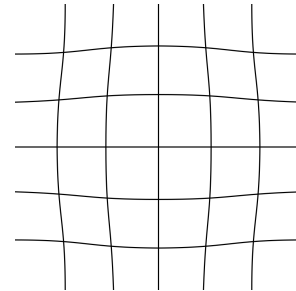
$$x' = x(1 + k_1\rho^2 + k_2\rho^4 + k_3\rho^6), \quad y' = y(1 + k_1\rho^2 + k_2\rho^4 + k_3\rho^6) \quad (4.11)$$



(a) Barrel Radial Distortion



(b) Pincushion Radial Distortion



(c) Mustache Radial Distortion

Where,  $\rho$  represents the radial distance from the principal point of the camera, while  $k_1$ ,  $k_2$ , and  $k_3$  are parameters that define the effect of radial distortion.

Specifically,  $k_1$  is generally the primary coefficient governing minor distortions. The coefficient  $k_2$  takes nonzero values when it is necessary to compensate for more pronounced distortions. Meanwhile, the coefficient  $k_3$  is less common and is employed in the correction of significantly distorted images.

An additional set of parameters, generally called higher-order radial coefficients, can be added to these. These coefficients are used to extend the polynomial radial distortion model (Equation 4.11) to the radial distortion model (Equation 4.12), allowing for the accurate handling of even more complex distortions.

$$x' = x \frac{(1 + k_1\rho^2 + k_2\rho^4 + k_3\rho^6)}{(1 + k_4\rho^2 + k_5\rho^4 + k_6\rho^6)}, \quad y' = y \frac{(1 + k_1\rho^2 + k_2\rho^4 + k_3\rho^6)}{(1 + k_4\rho^2 + k_5\rho^4 + k_6\rho^6)} \quad (4.12)$$

#### 4.1.2.2 Tangential Distortion

Tangential distortion typically produces less pronounced effects compared to radial distortion. It arises from an imperfect alignment of the lens with the film or sensor plane. This type of distortion occurs when the image appears shifted from its ideal position, resulting in a distortion that is not symmetric concerning the centre of the image (Figure 4.6a).

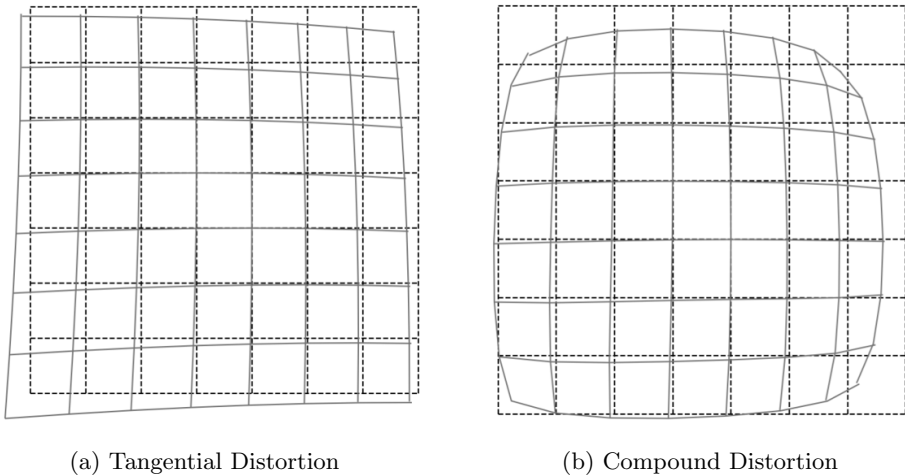
The tangential distortion model can be expressed as shown by Equation 4.13.

$$x' = x + [2p_1y + p_2(\rho^2 + 2x^2)], \quad y' = y + [p_1(\rho^2 + 2y^2) + 2p_2x] \quad (4.13)$$

Where  $p_1$  and  $p_2$  are the characteristic coefficients of the model.

In many cases, radial and tangential distortion are present simultaneously (Figure 4.6b). In many cases, the combination of the two models presented in Equation 4.14 is sufficient to describe the distortion in the image accurately, and no further corrections are needed.

$$\begin{aligned} x' &= x(1 + k_1\rho^2 + k_2\rho^4 + k_3\rho^6) + [2p_1y + p_2(\rho^2 + 2x^2)] \\ y' &= y(1 + k_1\rho^2 + k_2\rho^4 + k_3\rho^6) + [p_1(\rho^2 + 2y^2) + 2p_2x] \end{aligned} \quad (4.14)$$



#### 4.1.2.3 Thin-Prism Distortion

However, it may be necessary to account for additional distortion effects in more complex cases. These effects are generally represented within the thin-prism distortion model. Thin-prism distortion arises due to imperfections in the manufacturing and assembly of the lenses. These imperfections can cause the lens to deviate light unevenly, creating an angular distortion effect similar to an optical prism. This type of distortion is typically represented by Equation 4.15.

$$x' = s_1 r^2 + s_1 r^4, \quad y' = s_3 r^2 + s_4 r^4 \quad (4.15)$$

Where  $s_1$ ,  $s_2$ ,  $s_3$  and  $s_4$  are the coefficients of the model.

#### 4.1.2.4 Scheimpflug Principle

Although the three models presented above generally describe the most common types of distortion, it is important to consider a fourth effect. This type of distortion only appears when a Scheimpflug is used in the optical system. Scheimpflugs are a special type of lens that allows the camera sensor to be tilted so that an oblique plane can be focused. A simplified schematic of the working principle of the Scheimpflug is shown in Figure 4.7.

These tools are extremely useful in applications similar to those of interest. Nevertheless, it is important to consider that the sensor's tilt introduces additional distortion in the images. In Louhichi et al. 2007, a model was presented to account for this effect. This study proposes the introduction of two terms,  $\tau_x$  and  $\tau_y$ , which define two successive rotations,  $R(\tau_x, \tau_y)$ , as shown in Equation 4.16.

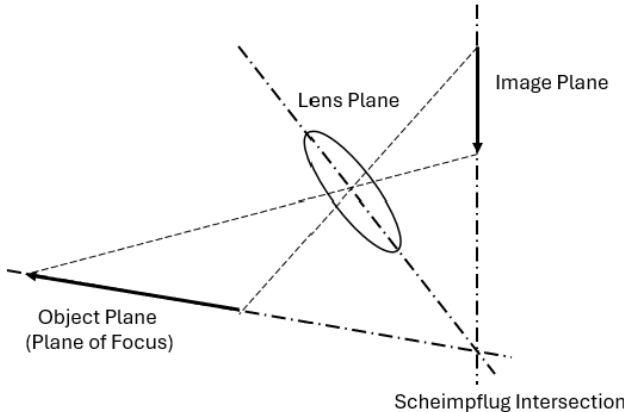


Figure 4.7: Characteristic angles of the Scheimpflug principle.

$$\begin{aligned}
 R(\tau_x, \tau_y) &= \begin{pmatrix} \cos(\tau_y) & 0 & -\sin(\tau_y) \\ 0 & 1 & 0 \\ \sin(\tau_y) & 0 & \cos(\tau_y) \end{pmatrix} \begin{pmatrix} 1 & 0 & 0 \\ 0 & \cos(\tau_x) & \sin(\tau_x) \\ 0 & -\sin(\tau_x) & \cos(\tau_x) \end{pmatrix} \\
 &= \begin{pmatrix} \cos(\tau_y) & \sin(\tau_y) \sin(\tau_x) & -\sin(\tau_y) \cos(\tau_x) \\ 0 & \cos(\tau_x) & \sin(\tau_x) \\ \sin(\tau_y) & -\cos(\tau_y) \sin(\tau_x) & \cos(\tau_y) \cos(\tau_x) \end{pmatrix}
 \end{aligned} \tag{4.16}$$

Using the matrix  $R(\tau_x, \tau_y)$ , it is possible to remap the distorted coordinates into the undistorted ones. Equation 4.17 expresses the relationship between distorted and undistorted point coordinates.

$$\begin{pmatrix} x' \\ y' \\ 1 \end{pmatrix} = \begin{pmatrix} R_{33}(\tau_x, \tau_y) & 0 & -R_{13}(\tau_x, \tau_y) \\ 0 & R_{33}(\tau_x, \tau_y) & -R_{23}(\tau_x, \tau_y) \\ 0 & 0 & 1 \end{pmatrix} R(\tau_x, \tau_y) \begin{pmatrix} x \\ y \\ 1 \end{pmatrix} \tag{4.17}$$

#### 4.1.2.5 Practical Applications

The distortion models presented can be combined to achieve more comprehensive and sophisticated models. However, assuming that the most complete model (which incorporates all coefficients) is always the most effective would be incorrect. On the contrary, the distortion model that minimizes reprojection errors varies each time cameras are calibrated and strongly depends on both the application type and experimental setup. For this reason, this work decided to repeat the calibration calculations for different models each time camera calibration was required. Specifically, four models based on the distortion present in the images were considered.

- The Polynomial Model (non-zero coefficients  $[k_1, k_2, k_3, [p_1, p_2]]$ )
- The Rational Model (non-zero coefficients  $[k_4, k_5, k_6]$ )

- The Thin-Prism Model (non-zero coefficients  $[s_1, s_2, s_3, s_4]$ )
- The Tilted Model (non-zero coefficients  $[\tau_x, \tau_y]$ )

Table 4.1 shows the distortion model combinations considered within this thesis.

Combinations	Polynomial Model	Rational Model	Thin Prism Model	Tilted Model
Model 0				
Model 1	✓			
Model 2	✓	✓		
Model 3	✓		✓	
Model 4	✓			✓
Model 5	✓	✓	✓	
Model 6	✓		✓	✓
Model 7	✓	✓		✓
Model 8	✓	✓	✓	✓

Table 4.1: Combinations of distortion models considered.

These coefficients can also serve as "error storages" in addition to modelling distortions caused by the lenses. By activating a distortion model, a certain number of additional coefficients are introduced to the intrinsic camera parameters. These additional parameters allow for partial compensation of errors generated by effects not directly accounted for by the models (e.g., the air-plexiglass-water interface).

### 4.1.3 Refraction Effects and Management

Although, in some cases, it is possible to obtain accurate results by handling refraction due to the plexiglass-water interface using only distortion models in general, it is better to address the problem explicitly.

First, clarifying the effects of light refraction through the tunnel windows is necessary. In this regard, a preliminary simplification can be introduced, reducing the problem's complexity while sacrificing minimal accuracy. By examining Table 4.2, it is observed that the difference between the refractive indices of water and plexiglass is relatively small. Additionally, the thickness of the tunnel windows (35 mm) is considerably smaller than the path that light rays travel in water.

Medium	Refractive Indices
Air	1.000293
PMMA (Plexiglas)	1.4896
Water	1.3330

Table 4.2: Materials Refractive Indices .

For these reasons, it is possible to neglect the change in material from plexiglass to water, considering the double interface as a single air-water interface.

As observed in Figures 4.8 and 4.9, the effect generated by the presence of the interface primarily depends on the angle between the camera sensor and the interface itself.

First, consider the case where the camera sensor and the interface are parallel. In this scenario, the real perspective rays are refracted due to Snell's law. The pinhole camera model cannot describe the refraction effect. Consequently, the

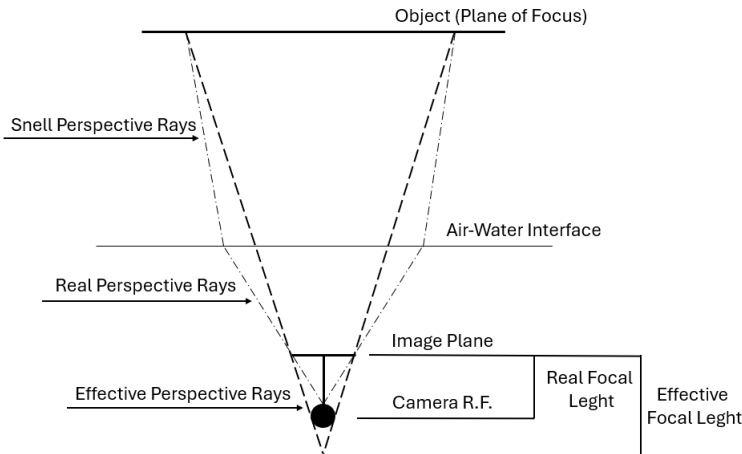


Figure 4.8: Refraction effect depending on the angle between the camera sensor and the air-water interface. Camera sensor parallel to air-water interface (Effect on Focal Length).

model (once calibrated) accounts for refraction by simply adopting an effective inclination of the perspective rays different from the actual one. Practically, this leads to overestimating the camera's focal length (Figure 4.8).

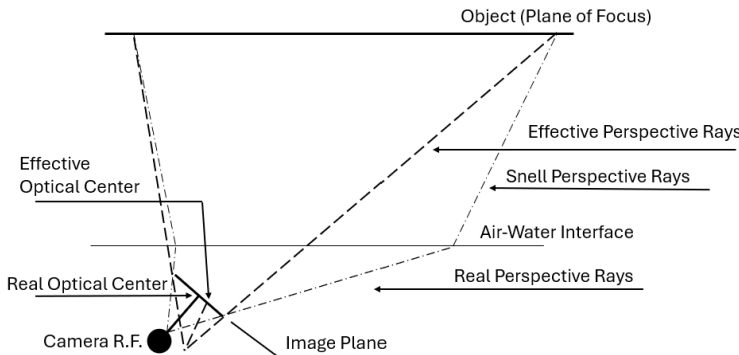


Figure 4.9: Refraction effect depending on the angle between the camera sensor and the air-water interface. Camera sensor non parallel to air-water interface (Effect on Principal Point).

The problem becomes even more complicated if the camera sensor and the air-water interface are not parallel. In this case, the refraction effect not only alters the estimation of focal length but also causes significant errors in identifying the camera's principal point. The erroneous position of the principal point tends to have a more severe consequence than errors in focal length estimation, as it often results in more significant re-projection errors. For this reason, commonly adopted solutions in the literature for handling interface effects focus primarily on accurately estimating the principal point. To maintain some flexibility in the experimental

setup, it is not feasible to force the alignment of camera sensors parallel to the cavitation tunnel windows. An effective and commonly adopted solution from the literature for restoring the parallelism between the camera sensor and the air-water interface involves prisms. These prisms are often made entirely of plexiglass or are hollow and filled with water (Figure 4.10).

By placing a prism with a base angle equal to the angle between the camera sensor and the air-water interface, a new interface parallel to the sensor is obtained. In this way, the error in estimating the camera's principal point is fully resolved, leaving only the issue of the focal length to be addressed.



Figure 4.10: Plexiglas prism.

Although an inaccurate estimate of the focal length is generally less problematic than errors in measuring the principal point, some considerations are still necessary. Firstly, it is essential to ensure that the error in this estimation is reasonable. In this regard, a very effective approach is positioning the camera as close as possible to the interface (e.g., the prism or window). This way, the distance the perspective rays must travel through air is minimized. The result is similar to that achieved by positioning the cameras directly underwater. Although placing the camera in direct contact with the interface would be the optimal solution, this is not always feasible. Considering the field of view and the available optics of the laboratory, it is often necessary to accept a certain distance between the cameras and the windows. In general, this does not pose a significant problem. As long as this distance does not become excessive, the resulting error can be managed through distortion models and the camera's intrinsic parameters, still allowing for high-quality measurements.

## 4.2 Camera Calibration

After selecting the camera model to base the measurement technique, it is necessary to proceed with calibration. Camera calibration is the process of defining both the camera's characteristics and its position in space. Calibration procedures can be divided into three categories depending on the number of cameras to calibrate.

When data from a single camera are required, the process is called mono calibration (Section 4.2.1). The purpose of mono calibration is to determine the intrinsic parameters of the camera, the distortion model coefficients, and the extrinsic parameters that relate the camera reference frame to the world reference frame.

When two cameras are calibrated as a stereo pair, the process is referred to as stereo calibration (Section 4.2.2). Finally, multiview calibration is used when three or more cameras must be calibrated simultaneously (Section 4.2.3). In these latter cases, in addition to determining the intrinsic parameters of each camera and their respective distortion coefficients, it is also necessary to obtain the information required to establish the relative positions between every possible pair of cameras.

The following sections provide a brief description of each of these procedures. The aim of these descriptions is to provide a solid foundation that clarifies the principles and reasoning underlying camera calibration. Furthermore, the errors affecting these procedures will be addressed to demonstrate how they have been managed and controlled. For a more formal and detailed description of these procedures, readers are referred to specialized texts such as R. Hartley and Zisserman 2003.

### 4.2.1 Mono Calibration

As previously mentioned, calibrating a camera in a monocular configuration involves determining all the characteristic coefficients of the projection model. To better clarify this concept, consider Equation 4.9. This equation generally allows for the projection of a three-dimensional point in the world reference system  $[X, Y, Z, 1]$  onto a pixel in the image reference system  $[u, v, 1]$ . The projection is based on the intrinsic parameters of the camera, contained in the matrix  $K$ , and the extrinsic parameters, represented by the rotation matrix  $R$  and the translation vector  $T$ . The same equation can be used to calibrate the camera by reversing the unknowns and parameters. Given the coordinates of the point in three-dimensional space and on the image plane, it is possible to deduce both the intrinsic and extrinsic parameters.

In this form, the problem defined by equation 4.9 is underdetermined. The entries of the perspective projection matrix (*PPM*  $[3 \times 4]$ ) represent twelve unknowns to be determined using only two equations (one for  $u$  and one for  $v$ ).

Resolving the problem clearly requires more than knowing the coordinates of a single point in both the world coordinate system and the image plane. For reasons that will be clarified later, practical applications often involve using numerous points.

Generally, this task is performed using a calibration pattern. Broadly speaking, a calibration pattern can be any object with easily recognizable features. In most cases, these objects are chessboards (Figure 4.11a) or dot grids (Figure 4.11b).

In this thesis, chessboard calibration patterns were used. Certain programming libraries specifically developed for computer vision tasks (OpenCV 2024) provide algorithms for detecting chessboard corners. When used correctly, these algorithms allow for determining point coordinates in the image plane with sub-pixel accuracy (Figure 4.12). Achieving this level of precision is essential to obtain low reprojection errors.

Identifying the chessboard corners in the image grants access to the coordinates  $[u, v, 1]$  for a set of points. However, to apply Equation 4.9, the coordinates in the world coordinate system  $[X, Y, Z]$  are still required.

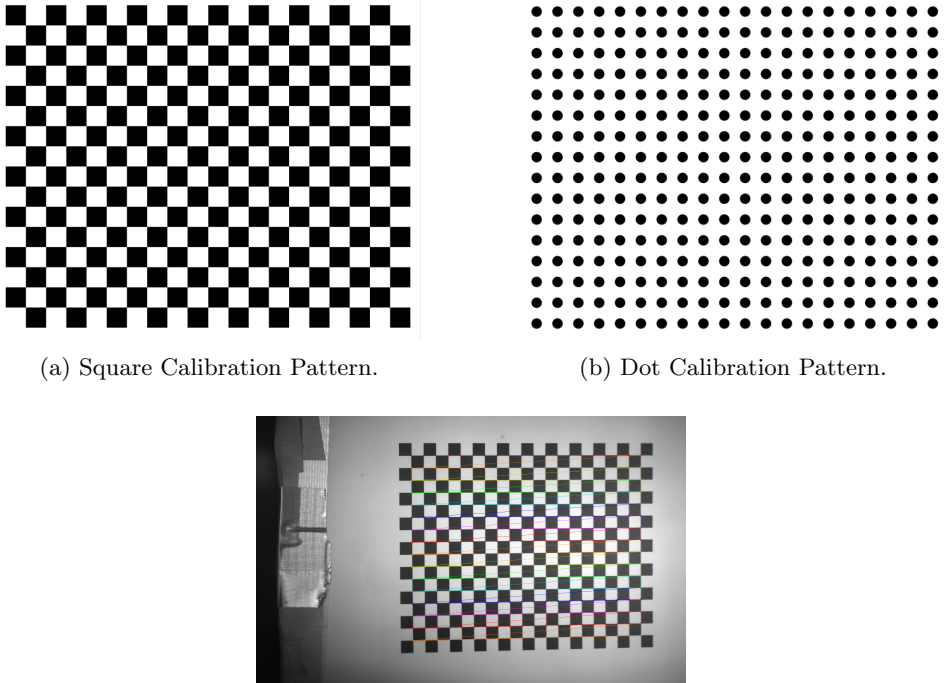


Figure 4.12: Chessboard Corners detected in a Calibration Pattern

As previously mentioned, the world reference system is entirely arbitrary, and its position can be freely chosen. Typically, the origin of the world reference system is placed at the top-left corner of the pattern (as shown in Figure 4.13). Generally, the world reference system is oriented such that the  $X$  and  $Y$  axes lie on the plane of the pattern, while the  $Z$  axis is orthogonal to and extends outward from it. As will be demonstrated later, this arrangement significantly simplifies the calibration procedure.

#### 4.2.1.1 Theoretical Aspects

After defining the reference systems and identifying the corners of the calibration pattern both in the image and the world, the geometric relationship between the two systems can be established. Fullfill this task means determining the coefficients of Equation 4.9.

This equation includes twelve coefficients, although not all of them are independent. The matrix  $K$  depends on four primary parameters: the focal lengths  $f_x$  and  $f_y$ , and the coordinates of the principal point  $c_x$ ,  $c_y$ . Three rotation angles uniquely determine the rotation matrix  $R$ . Finally, the translation vector  $T$  consists of three components. Consequently, the total number of unknowns is not twelve but ten.

Equation 4.9 describes a general perspective projection. However, adopting a planar calibration pattern can be interpreted as a plane homography. The plane homography is a specific perspective projection that defines the mapping between points on one plane and those on another.

In this particular case, the plane homography represents the relationship be-

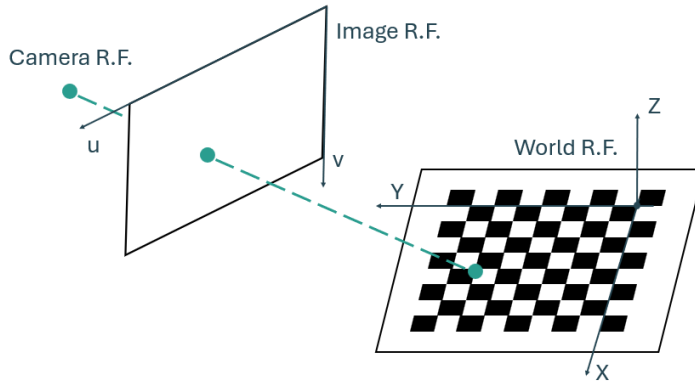


Figure 4.13: Positioning of World Reference Frame on a Calibration Pattern

tween points on the image plane and those on the pattern. If  $m$  denotes the homogeneous coordinates of a point on the image plane,  $[u, v, 1]$ , and  $M$  denotes the homogeneous coordinates of the same point in the world reference system,  $[X, Y, Z, 1]$ , the plane homography assumes the form given in Equation 4.18.

$$m = sHM \quad (4.18)$$

In the present case, this equation assumes a physical meaning, and the homography matrix  $H$  represents the perspective projection matrix  $PPM$ . The term  $s$  is a scaling factor required because homogeneous coordinates are defined up to a scaling factor. In these terms, Equation 4.18 takes the form of Equation 4.19.

$$m = sK(R \mid T)M \quad (4.19)$$

By choosing to position the world reference frame as indicated in 4.13, the problem is considerably simplified. Indeed, by adopting this reference frame, all the calibration pattern corners lie on the  $XY$  plane and thus have a null  $Z$  coordinate. This implies that the third column of the rotation-translation matrix  $(R \mid T)$  is not necessary, and the coordinates  $M = [X, Y, Z, 1]$  can be reduced to  $\tilde{M} = [X, Y, 1]$ , leading to Equation 4.20.

$$m = sK(r_1 \ r_2 \mid T)\tilde{M} \quad (4.20)$$

Where  $r_1$  and  $r_2$  represent the first and second columns of the rotation matrix, respectively. In this form, the planar homography  $H = sK(r_1 \ r_2 \mid T)$  becomes a  $[3 \times 3]$  matrix. Consequently, the number of unknowns to be determined reduces from ten to nine.

Typically, the scaling factor  $s$  is fixed to normalize the matrix  $H$  and ensure  $H_{33} = 1$ . This choice imposes an additional constraint on the problem, reducing the number of unknowns from nine to eight.

As previously noted, perspective projection allows us to write two equations (one for  $u$  and one for  $v$ ) for each point with known coordinates in both the image plane and the world coordinate system. It is thus evident that the minimum number of points required to solve the system is four.

Although four points are sufficient from a mathematical perspective to determine the components of the matrix  $H$ , in practical contexts, patterns with many

points are commonly used. Indeed, using only four points would make the solution highly sensitive to small errors. A slight inaccuracy in the localization of any of these points would result in significant errors in the calculated homography. In contrast, using patterns with many points allows for optimization techniques, enabling the minimization of the overall projection error and improving the robustness and accuracy of the process.

Once the matrix  $H$  components have been determined, the calibration procedure cannot be considered complete. Indeed, it is still necessary to separate the intrinsic parameters of the camera (the matrix  $K$ ) from the extrinsic parameters (the rotation-translation matrix ( $R$  |  $T$ )). This distinction is fundamental to isolating the camera's optical properties from those related to its position and orientation in space. To define this distinction, it is necessary to use a series of multiple views of the calibration pattern.

As previously discussed, a single pose of the pattern can be associated with ten unknowns (the components of the perspective projection matrix  $PPM$ ) and eight constraints (defined through the homography matrix  $H$ ). The perspective projection matrix can be written as the product of the intrinsic and extrinsic parameters. The camera's intrinsic parameters remain unchanged with varying observed scenes and thus remain invariant across different poses of the calibration pattern. On the other hand, the rotation-translation depends on how the world reference frame is defined, i.e., how the pattern is positioned.

This implies that four of the ten unknowns remain fixed across varying views of the pattern, while eight new constraints can be formulated for each additional pose. Therefore, a sufficient number of views of the pattern can separate the intrinsic from the extrinsic parameters. The minimum number of views required for this separation is determined by Equation 4.21.

$$6 \cdot \alpha + 4 = 8 \cdot \alpha \quad (4.21)$$

In which the terms on the left-hand side represent the number of unknowns varying with the number of calibration pattern positions considered. The right-hand side indicates the number of degrees of freedom. This relationship shows that two different poses of the calibration pattern would be sufficient to separate intrinsic and extrinsic terms. However, similar to the number of points, using only two poses does not guarantee a good calibration result. Many different positions are utilized to achieve the solution by applying an optimization algorithm.

This principle is precisely the basis of the algorithm proposed by Zhang 2000. This technique is by far the most widely used in camera calibration. It suggests utilizing the different homographies obtained from multiple poses to provide an initial estimate of the camera's intrinsic parameters and distortion coefficients. Subsequently, an iterative optimization process, often based on the Levenberg-Marquardt algorithm, is employed to minimize reprojection errors, i.e., the distance between the image points projected according to the camera model and the detected image points.

In addition to optimizing the calculation of the camera's intrinsic parameters, access to a much larger number of points distributed across the entire image plane from many different pattern poses allows for more accurate modeling of lens distortions and improves the precision of distortion coefficients.

### 4.2.1.2 Accuracy Validation

To ensure the successful calibration of cameras, the performance at each step must be verified. For this reason, an analysis of the accuracy achieved will be provided at the end of each section discussing a calibration step.

Regarding monocular calibration, three main factors must be considered. The first of these is the mean reprojection error. The mean reprojection error is the average distance, expressed in pixels, between the world points projected onto the image through the camera model and the corresponding points actually detected in the image. Thus, it provides a good representation of the accuracy with which the estimated intrinsic and extrinsic parameters reproduce the observed geometry. Figure 4.14 shows an example of mean reprojection error for a certain camera, varying the distortion model.

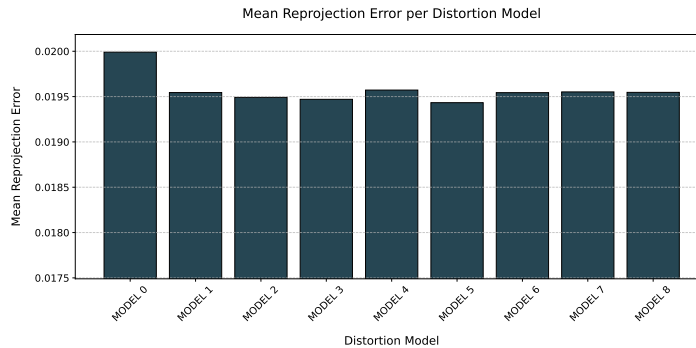


Figure 4.14: Mean Reprojection Error per Distortion Model (Table 4.1)

This figure shows that, although each tested distortion model produces satisfactory results, some models are more performant than others. In addition to the mean reprojection error, it is important to consider the difference between the calculated intrinsic parameters and their theoretical counterparts.

Given that the cameras' pixels are square in shape, the focal lengths  $f_x$  and  $f_y$  must be equal. Figure 4.15 shows the percentage differences between the focal lengths  $f_x - f_y$ . This length should theoretically be zero.

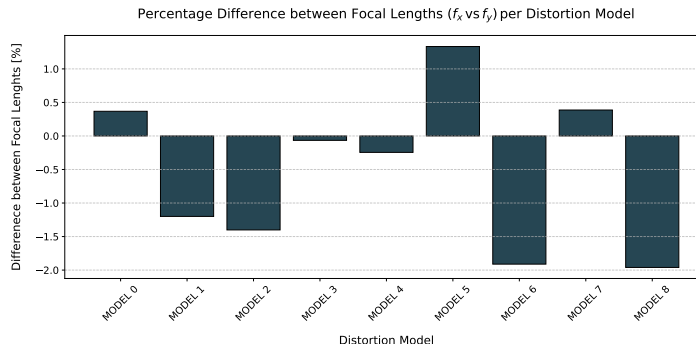


Figure 4.15: Focal Lengths Difference per Distortion Model (Table 4.1)

The last parameter to consider in evaluating the accuracy of calibration is the

coordinates of the principal point of the image. Theoretically, this point should be located at the centre of the image plane. The position of the principal point is an extremely important parameter in camera calibration as it defines the camera ray bundle. Figure 4.16 shows the difference between the calculated principal point coordinates  $c_x$  and  $c_y$  and their theoretical values (the sensor's centre) for the different distortion models.

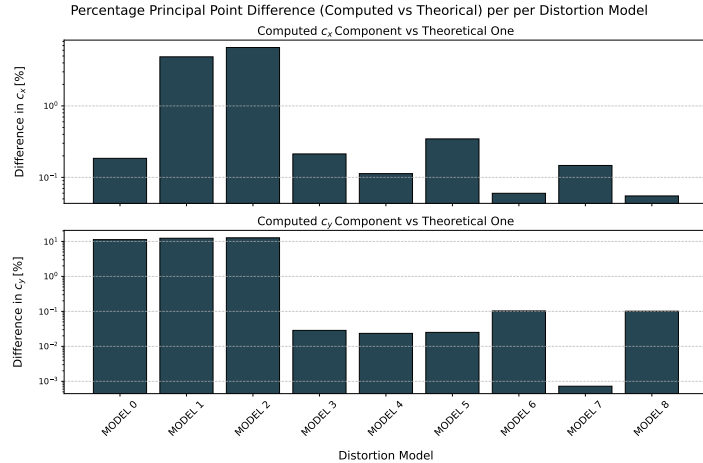


Figure 4.16: Principal Point Difference per Distortion Model (Table 4.1)

The observed differences in intrinsic parameters do not indicate the precision of the calibration performed but rather its validity. Indeed, if these differences become excessive, it is probable that the optimization process has converged to non-optimal parameters, which, while resulting in acceptable reprojection errors, are not truly representative of the camera.

#### 4.2.1.3 Warp Correction of Tunnel Windows

The steps shown up to this point allow calibration of a camera operating in a homogeneous medium. However, obtaining a valid calibration in the cavitation tunnel environment may require additional considerations.

Cavitation tests are conducted by applying a vacuum to the tunnel. This depression acts on the tunnel structures, pushing them inward. For this reason, during cavitation tests, the tunnel windows are not flat surfaces but instead become slightly curved inward. The bending of the windows results in further deformation of the path of the perspective rays. Addressing this issue is important to avoid significant errors.

First, it is necessary to consider the actual extent of the bending to which the windows are subjected when the tunnel is under vacuum. The maximum deformation of the windows, measured (using a comparator like the one shown in figure 4.17) at the centre of the windows, is approximately 0.8 mm.

Calibrating the camera directly while the tunnel is under vacuum could theoretically enable the obtaining of a calibration model capable of handling the nonlinearities introduced by this additional deviation of the optical rays. However, from a practical standpoint, performing the calibration under these conditions is unfea-



Figure 4.17: Measurement of the Tunnel Window Deformation

sible. Therefore, a first calibration was carried out by positioning the reference pattern in water while keeping the tunnel at atmospheric pressure. Subsequently, a corrective transformation was applied to account for the bending of the windows caused by the vacuum application.

A homography matrix was calculated for each of the cavitation indices under which the experiments were conducted. Two images of the calibration pattern were used to compute each matrix. The first image was captured under atmospheric conditions, while the second was captured with the tunnel under vacuum. Letting  $m$  represent the corners of the pattern in the atmospheric image and  $m'$  the corners from the vacuum image, the homography can be computed as shown in Equation 4.22.

$$m = H m' \quad (4.22)$$

In this way, the homography provides a map that allows for associating the coordinates of the points when the tunnel is in depression with their coordinates under atmospheric conditions. By remapping the points analyzed during the measurements through the homography matrix  $H$ , the distortion effect caused by the windows can be removed, and the validity of the calibration procedure previously described can be restored.

In practical cases, the effectiveness of the homography presents some limitations. Firstly, it must be considered that this transformation is linear and, therefore, cannot correct strongly nonlinear geometric distortions. For this reason, measurements will still be subject to a certain margin of error, albeit reduced. To minimize this error, it is better to position the cameras as close as possible to the

tunnel windows. This configuration reduces the camera's field of view, limiting the portion of the window captured and decreasing the impact of surface curvature on the quality of the acquired image.

Therefore, there exists a maximum distance from the windows beyond which the measurements become inaccurate. This occurs both due to window deformation and errors in the focal length estimation caused by the interface.

Even when the camera is placed very close to the window, the effectiveness of the homography must be discussed. Indeed, under these conditions, correction becomes less necessary due to the above reasons. At the same time, it still introduces an additional level of complexity into the system, which could degrade the measurement rather than improve it.

To evaluate these aspects, some analyses must be conducted. For this purpose, in addition to the homography, another matrix  $S$  has been calculated. This matrix was obtained by remapping the corners of the pattern from an image acquired under atmospheric conditions back to themselves (as shown in Equation 4.23).

$$m = S m \quad (4.23)$$

The effect of the matrix  $S$  on the coordinates of the points should obviously be identical to that of an identity matrix. The effectiveness of the homography can be analyzed using a new pair of images acquired under different conditions. Applying the homography to the corners of the pattern detected in the image taken under vacuum conditions allows for estimating their corresponding positions under atmospheric conditions. These estimated points can be compared with the actual corners detected in the image acquired under atmospheric conditions. The comparison allows for the calculation of an average error representing the homographic transformation's efficacy.

A similar analysis can be conducted by applying the matrix  $S$  to the corners detected in the image under normal atmospheric conditions. In this case, the comparison between the estimated position of the points, obtained downstream of the transformation, and their actual position allows for assessing the error introduced by the application of  $S$ .

Finally, the displacement of the corners from the vacuum to the atmospheric condition can be evaluated. This corresponds to calculating the average distance between homologous corners between images acquired under different conditions without applying any transformation (Equation 4.24).

$$m = m' \quad (4.24)$$

The average distance between homologous corner pairs provides important information for understanding the magnitude of deformation effects on windows.

Table 4.3 presents an example of these average errors.

Transformation	Mean Error [pix]
H	0.08
S	0.11
-	0.19

Table 4.3: Mean Errors in Warp Correction of Tunnel Windows.

If the mean error after applying the homography transformation  $H$  is high, it indicates that the images contain high nonlinear transformations. In this case, the experimental setup must be modified.

On the other hand, when the residual error is relatively low, the measurement can be considered valid. However, in some cases, such as the one in the example, applying the homography may not be necessary.

By examining Table 4.3, it is observed that the mean error introduced by applying matrix  $S$  is similar to the error that would be made by neglecting the effect of window deformation. This suggests that the increase in measurement accuracy obtained by applying the homography is mostly compensated by the further complexity of the model.

## 4.2.2 Stereo Calibration

Stereo calibration is a process that allows the determination of the geometric relationship between two cameras. This relationship is necessary for analyzing and reconstructing the depth of objects in a three-dimensional scene. This procedure aims to define the extrinsic parameters, i.e., the relative position and orientation of the two cameras. The intrinsic parameters of each camera, previously determined through monocular calibration, remain unchanged.

### 4.2.2.1 Epiplar Geometry

Before describing the stereo calibration procedure, it is necessary to introduce the concepts of epipolar geometry. Epipolar geometry describes the relationship between two images capturing the same scene from different viewpoints. Specifically, it defines the relationship between the two projections of the same 3D point onto their respective image planes.

From a mathematical standpoint, this relationship can be defined through the essential matrix  $E$ . This matrix connects the world coordinates of a point observed from two different camera reference frames. Adding to this, the information from the camera's intrinsic parameters allows for establishing the relationship between the points on their respective image planes (measured in pixels). This relationship is described by the fundamental matrix  $F$ .

Understanding the definition of these matrices requires introducing the concept of the epipolar plane. Consider a stereo system comprising two cameras, indicated by subscript 1 and 2. A point in the world reference frame  $M$ , along with the origins of the reference frames of the two cameras (denoted  $\omega_1$  and  $\omega_2$ ), defines a plane. This plane is known as the epipolar plane  $\Pi$ .

The intersection of the epipolar plane  $\Pi$  with the image plane of each camera generates a line known as the epipolar line. For each image, all epipolar lines converge at a common point, the epipole. Therefore, each image is characterized by a specific epipole, denoted as  $e_1$  and  $e_2$ , respectively. Lastly, the segment connecting the optical centers of the two cameras, corresponding to the origins  $\omega_1$  and  $\omega_2$ , is called the baseline.

A schematic illustration of the elements underlying epipolar geometry is shown in Figure 4.18.

Since not only the optical centres of the cameras ( $\omega_1$  and  $\omega_2$ ) lie on the epipolar plane  $\Pi$ , but also the projections of point  $M$  onto the image planes ( $m_1$ ,  $m_2$ ), it follows that, given a point in three-dimensional space ( $M$ ) and its projection

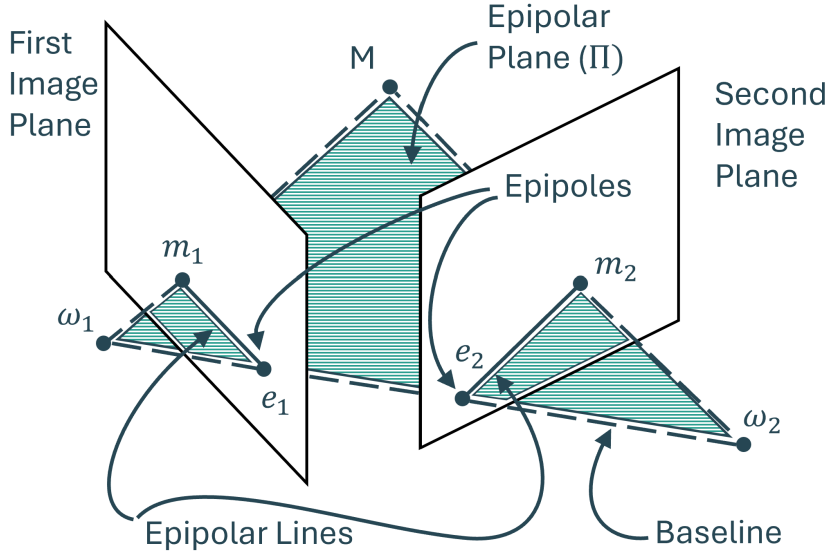


Figure 4.18: Epipolar Geometry Elements

onto one image plane (e.g.,  $m_1$ ), the projection onto the other plane (i.e., point  $m_2$ ) is constrained to lie on the corresponding epipolar line. This constraint is extremely useful in computer vision, as it significantly reduces the difficulty of finding corresponding points in different images, simplifying the three-dimensional reconstruction process.

The epipolar geometry elements introduced above can be used to define the relationship between corresponding points on the two image planes denoted as  $m_1$  and  $m_2$ . To achieve this, it is first necessary to consider a point  $M$  in the world reference frame. Let  $PPM_1$  and  $PPM_2$  denote the perspective projection matrices; the points  $m_1$  and  $m_2$  will satisfy Equation 4.25.

$$\begin{aligned}\lambda_1 m_1 &= PPM_1 M \\ \lambda_2 m_2 &= PPM_2 M\end{aligned}\quad (4.25)$$

Where  $\lambda_1$  and  $\lambda_2$  represent scale factors derived from homogeneous coordinates. As before, the world reference frame can be defined arbitrarily. In this case, aligning it with one of the camera's reference frames is convenient. For example, the world reference frame can coincide with the first camera reference frame, as shown in Figure 4.19.

Under this hypothesis, Equation 4.25 can be reformulated as shown in Equation 4.26. In this equation, the terms  $K_1$  and  $K_2$  represent the matrices of the respective cameras containing the intrinsic parameters. The rotation matrix  $R$  and the translation vector  $T$  define the position of the first camera reference frame (i.e., the world reference frame) with respect to the second camera one.

$$\begin{aligned}\lambda_1 m_1 &= K_1 [I \ 0] M \\ \lambda_2 m_2 &= K_2 [R \ T] M\end{aligned}\quad (4.26)$$

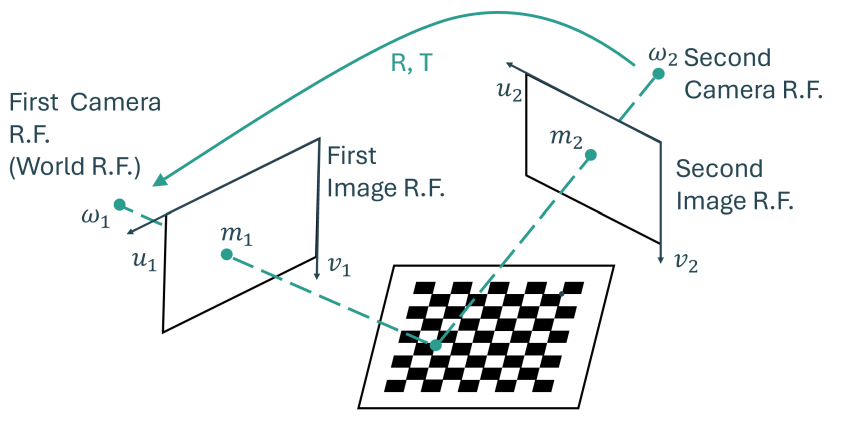


Figure 4.19: Relationship between Stereo Camera Reference Frames

Developing and comparing these equations can be rewritten in the form shown in Equation 4.27.

$$\begin{aligned} \lambda_1 K_1^{-1} m_1 &= \hat{M} \\ \lambda_2 m_2 &= K_2(R\hat{M} + T) \end{aligned} \quad \longrightarrow \lambda_2 m_2 = \lambda_1 K_2 R K_1^{-1} m_1 + K_2 T \quad (4.27)$$

In which  $\hat{M}$  is defined as  $M = [\hat{M} \ 1]^T$ , allowing the decomposition of the extrinsic term matrices. By further expanding Equation 4.27, the form presented in Equation 4.28 is obtained.

$$\lambda_2 K_2^{-1} m_2 = \lambda_1 R K_1^{-1} m_1 + T \quad (4.28)$$

From a geometric perspective, this expression indicates that the vector on the left-hand side ( $\lambda_2 K_2^{-1} m_2$ ) is a linear combination of the two vectors on the right-hand side ( $\lambda_1 R K_1^{-1} m_1 + T$ ). This property implies that the three vectors are coplanar and all lie on the epipolar plane  $\Pi$ . The vector  $T \times R K_1^{-1} m_1$  identifies the normal vector to the plane  $\Pi$ . By taking the scalar product of the elements of Equation 4.28 with this vector, Equation 4.29 is validated.

$$\lambda_2 (K_2^{-1} m_2)^T (T \times R K_1^{-1} m_1) = 0 \quad (4.29)$$

The cross-product ( $T \times$ ) can be rewritten as a matrix product by introducing an auxiliary matrix  $[T]_x$ , as shown in Equation 4.30.

$$[T]_x = \begin{pmatrix} 0 & -T_z & T_y \\ T_z & 0 & -T_x \\ -T_y & T_x & 0 \end{pmatrix} \quad (4.30)$$

In which  $[T_x, T_y, T_z]$  are the components of the vector  $T$ . In this way, Equation 4.29 takes the form shown in Equation 4.31..

$$m_2^T (K_2^{-T} [T]_x R K_1^{-1}) m_1 = 0 \quad (4.31)$$

The matrix that relates the coordinates of the projections of the world point  $M$  onto the two image planes ( $m_1$  and  $m_2$ ) can therefore be referred to as the fundamental matrix  $F$  and expressed through Equation 4.32.

$$F = (K_2^{-T}[T]_x R K_1^{-1}) \quad (4.32)$$

If the camera matrices ( $K_1$ ,  $K_2$ ) are known, the intrinsic parameters can be decoupled from those that define the relative position of the two reference systems. Let  $\hat{m}_1$  be the coordinates of point  $M$  observed from the first camera's reference system, and let  $\hat{m}_2$  be the coordinates of the same point seen through the second camera's reference system. In these terms, Equation 4.31 takes the form of Equation 4.33.

$$(K_2^{-1}m_2)^T[T]_x R (K_1^{-1}m_1) = \hat{m}_1^T[T]_x R \hat{m}_2 = 0 \quad (4.33)$$

The essential matrix can thus be defined, as shown in Equation 4.34.

$$E = [T]_x R \quad (4.34)$$

Knowing the fundamental matrix  $F$ , it is possible to define, for a given point  $m_1$  in one image, the corresponding epipolar line in the other image of the stereo system. The epipolar lines  $l_2$  and  $l_1$ , corresponding to  $m_1$  and  $m_2$  in the first and second images, respectively, can be expressed using Equation 4.35.

$$\begin{aligned} l_2 &= Fm_1 \\ l_1 &= F^T m_2 \end{aligned} \quad (4.35)$$

#### 4.2.2.2 Theoretical Aspects

In the previous section, the geometrical concepts underlying a stereo camera dipole were introduced. This section provides the practical steps to calculate the essential matrix  $E$  and the fundamental matrix  $F$ .

Like the mono camera calibration, this procedure requires knowledge of the positions of a certain number of points in the world reference frame and their counterparts in the images. Again, a calibration pattern is used to identify these points easily.

By placing the world reference frame as shown in Figure 4.20, each corner  $M$  of the calibration pattern, when projected onto one of the camera image planes, can be described using Equation 4.36.

$$\begin{aligned} m_1 &= K_1 (R_1 \ T_1) M \longrightarrow \hat{m}_1 = (R_1 \ T_1) M = R_1 \hat{M} + T_1 \\ m_2 &= K_2 (R_2 \ T_2) M \longrightarrow \hat{m}_2 = (R_2 \ T_2) M = R_2 \hat{M} + T_2 \end{aligned} \quad (4.36)$$

Observing Figure 4.20, it is evident how the roto-translation matrices  $(R_1 \ T_1)$  and  $(R_2 \ T_2)$  are related. This relationship can be expressed by Equation 4.37.

$$\begin{aligned} R &= R_2 R_1^T \\ T &= T_2 - R T_1 \end{aligned} \quad (4.37)$$

Calculating the rigid-body transformation  $(R \ T)$  that identifies the reference frame of the first camera concerning the second requires the knowledge of a certain number of corresponding points in the image planes and the world coordinate system.

To determine the minimum number of points needed, we can consider the fundamental matrix  $F$ . The matrix  $F$  is a  $[3 \times 3]$  matrix composed of nine elements.

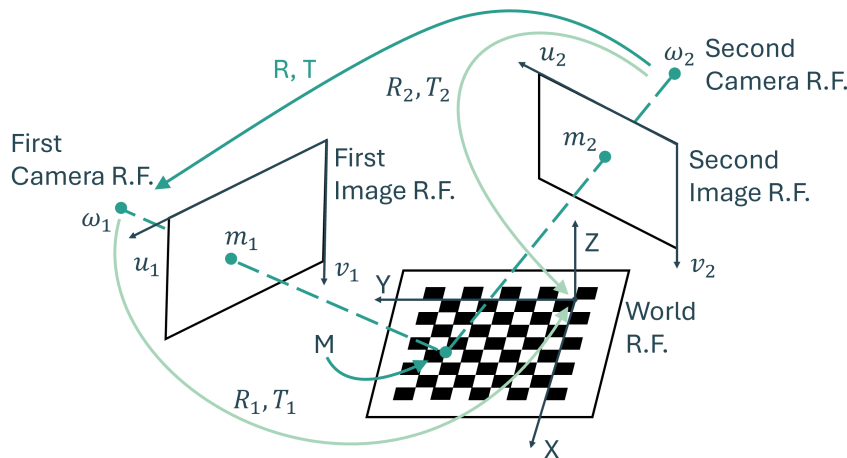


Figure 4.20: Relative Orientation between Cameras and World Reference Frames

However, it is defined up to a scale factor since it is expressed in homogeneous coordinates. This implies that the matrix  $F$  effectively has only eight degrees of freedom.

Therefore, identifying at least eight corresponding points between the two camera image planes allows for the computation of the fundamental matrix (since each point grants a constraint).

Observing Equation 4.32, it can be noticed that the fundamental matrix  $F$  must have a rank of two ( $\text{rank}(F) = 2$ ). In fact, the skew-symmetric matrix  $[T]_x$  has a rank of two by construction. This implies that the essential matrix has only seven degrees of freedom. However, in practical cases, many points are utilized to use optimization algorithms to obtain more precise and robust solutions.

Furthermore, as previously discussed in the context of mono camera calibration, by using different poses of the pattern, the fundamental matrix  $K$  can be decomposed into the camera matrices ( $K_1$  and  $K_2$ ) and the essential matrix  $E$ .

This way, the solution obtained is optimized within the spatial region where the pattern was moved during calibration. Thus, the calculated perspective matrices are valid only within that volume, while deviations from it produce progressively less accurate results.

#### 4.2.2.3 Accuracy Validation

In this thesis work, the accuracy of stereo calibration was assessed using two main parameters.

First, the root mean square reprojection error (in pixels) was analyzed, considering the individual cameras and their geometric relationship. Figure 4.21 presents an example of a calibration, showing the root mean square errors for each of the distortion models considered.

For single cameras, the root mean square (RMS) error is calculated by considering the Euclidean distance between the points detected in the image during the calibration process and the world points projected through the computed camera models. This value indicates the accuracy of the camera parameters describing its

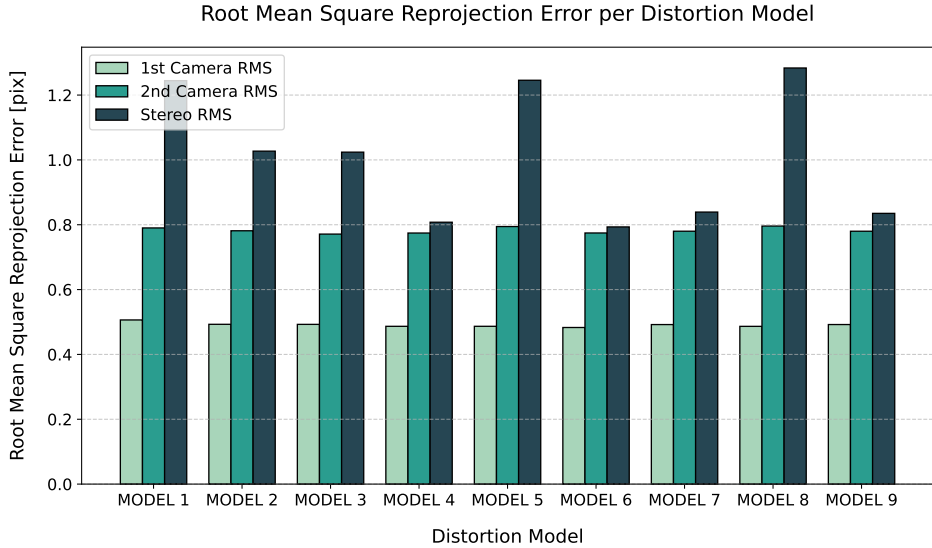


Figure 4.21: Mono and Stereo RMS Reprojection Error per Distortion Model (Table 4.1)

optical geometry. The geometric relationship between the two cameras (rotation and translation parameters) must be observed to assess the stereo dipole's characteristic mean square error. In this case, the coherence between the points of one camera and those of the other is evaluated, i.e. assessing the consistency of the epipolar constraint  $m_2^T F m_1 = 0$  for each pair of homologous points. In other words, for each pair of homologous points ( $m_1, m_2$ ), the distance between the line  $l_2 = F m_1$  and the point  $m_2$  is calculated. This is the distance between the epipolar line that the point  $m_1$  draws in the plane of the second camera and the point  $m_2$  through which it should pass. This error allows for verifying how accurately the stereo system is able to represent the spatial configuration of the points.

Generally, for calibrations conducted in homogeneous media, an RMS error of approximately 0.2 pixels is considered optimal, while an RMS error below one pixel is considered satisfactory. However, in the context of the cavitation tunnel, numerous environmental challenges can potentially lead to higher errors. Nonetheless, the RMS values obtained are widely acceptable. Indeed, in many distortion models, all three RMS values are below one pixel, confirming precise and robust calibration. This suggests that the difficulties associated with the cavitation tunnel environment do not significantly compromise the calibration quality, ensuring reliable and accurate results.

However, to ensure accuracy, it is important to consider both the reprojection errors and the triangulation errors shown in 4.22. To define the triangulation error characterizing the calibration of a stereo pair, it is first necessary to consider a pair of homologous points on the image planes ( $m_1$  and  $m_2$ ) and reproject them into space. The procedure of reprojection from images to the world coordinate system is known as triangulation. It will be described in detail in the following of this chapter (Section 4.3).

During the reprojection phase, it is essential to account for the optical distor-

tions present in the images and correct them using one of the models considered (Table 4.1).

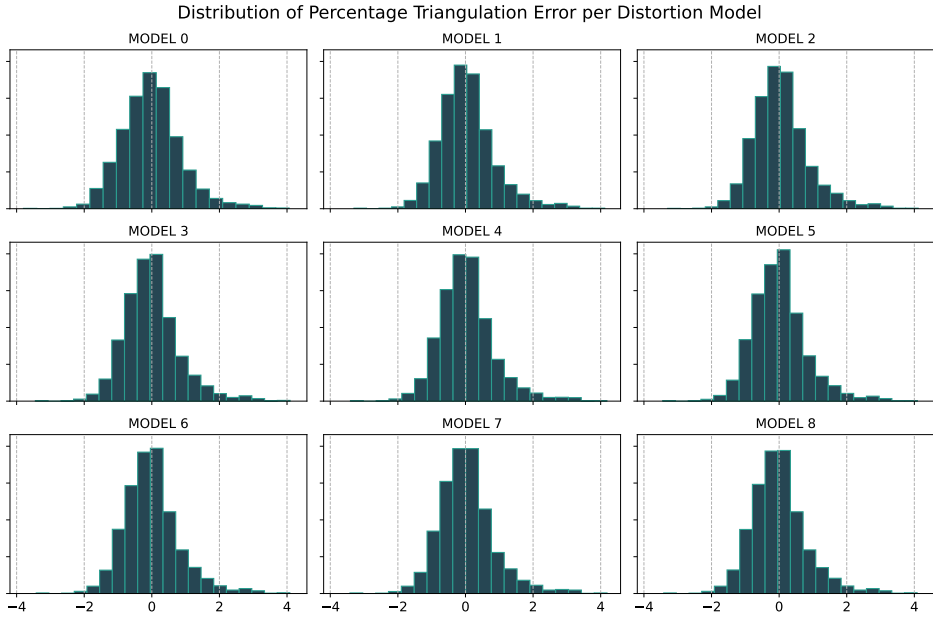


Figure 4.22: Distribution of Percentage Triangulation Error per Distortion Model (Table 4.1)

To ensure the reliability of error analysis, it is a good practice to use a different image dataset (consisting of various poses of the calibration pattern) than the one employed to define the model. The reprojection of a pair of homologous points ( $m_1$  and  $m_2$ ) identifies a point in the three-dimensional world,  $M$ . By projecting the corners of an entire calibration pattern, it is possible to evaluate the mutual distance between two adjacent 3D corners. The measured distance can then be compared with the distance between the adjacent corners of the physical object. A percentage triangulation error can be defined for each pair of adjacent corners based on the difference between these distances. Repeating this analysis for different poses of the pattern allows for validating the model with data that spans the entire calibrated volume.

The result of this analysis is a series of statistical distributions (one for each of the distortion models considered). If calculated using a sufficient number of images, these distributions provide valuable insights into the accuracy of the calibration. Furthermore, they allow selecting the most suitable distortion model for the specific case.

To synthesize the information contained in these statistical distributions, key metrics such as statistical moments, maximum error, or the percentage of outliers evaluated using a method like RANSAC (Fischler and Bolles 1981) are typically employed. This approach enables the selection of the desired model by considering not only the mean error but also the distribution of data around it. Additionally, these considerations allow for the imposing of constraints on the maximum error or the acceptable level of contamination by outliers. Table 4.4 provides an example

of these metrics as they vary across the different distortion models considered.

Model	Mean [%]	Max [%]	Std. Dev.	Skewness	Kurtosis	Outliers [%]
Model 0	-0.0096	4.061	0.887	0.517	1.374	0.854
Model 1	0.0554	4.120	0.825	0.829	1.981	1.208
Model 2	0.0540	4.113	0.820	0.824	1.976	1.208
Model 3	0.0001	4.090	0.822	0.799	2.046	2.541
Model 4	0.0388	4.184	0.819	0.827	2.204	1.271
Model 5	0.0070	4.089	0.815	0.800	2.069	1.250
Model 6	-0.0031	4.083	0.822	0.797	2.029	1.250
Model 7	0.0391	4.189	0.819	0.831	2.224	1.271
Model 8	-0.0030	4.083	0.821	0.797	2.026	1.250

Table 4.4: Statistical Metrics for Different Distortion Models. Metrics include mean, maximum value, standard deviation (Std. Dev.), skewness, kurtosis, and percentage of outliers.

The analysis can be conducted either by considering the application of the homographic transformation  $H$ , described in Section 4.2.1.3, or by excluding it. This approach allows for a comparison of the results obtained in both cases, evaluating the impact of this transformation on the overall performance of the triangulation process. The choice to apply  $H$  can be guided by analyzing the results, allowing for determining if it significantly improves the quality of the reconstructions or not.

### 4.2.3 Multiview Calibration

Generally, multiple cameras significantly enhance most computer vision techniques aimed at reconstructing objects in three-dimensional space. As will be extensively discussed in the section dedicated to the description of these techniques (§4.3), simultaneously employing more than two cameras allows for the imposition of a larger number of constraints on each point reprojected in space. Consequently, the position of such points is optimized, leading to increased precision.

Moreover, the more cameras used in the measurement process, the more viewpoints become available. Observing an object from multiple perspectives enables a more comprehensive understanding of its shape, resulting in a more faithful reconstruction. To utilize multiple cameras simultaneously, it is possible to repeat the procedure used for stereo calibration several times. Consider, for example, a system of three cameras denoted by subscripts 1, 2, and 3, respectively. This system shown in Figure 4.23 represents the simplest example of a multi-camera system.

Using the concepts of stereo calibration allows for calculating the relationship that links the second camera reference frame to the first camera one. This relationship would be formalized in the fundamental matrix  $F_{2,1}$ . The same process could be applied to the third camera, obtaining the fundamental matrix  $F_{3,1}$ .

Although this approach is not formally incorrect, it is highly suboptimal and often results in significant reprojection errors. This occurs because relying solely on the concepts of stereo calibration neglects several pieces of information contained within the multi-camera system. To understand how to extract and utilize this information, it is first necessary to introduce the concept of the epipolar graph.

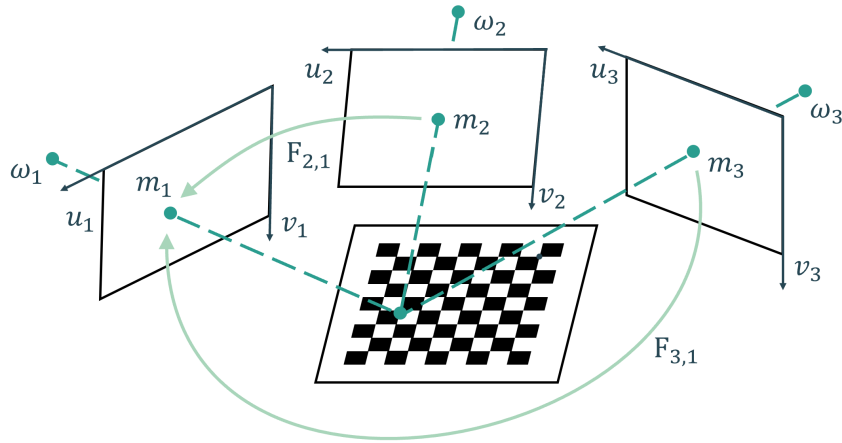


Figure 4.23: Relationship between Cameras in a Multicamera System

#### 4.2.3.1 Epiolar Graph

Consider a set of  $Z > 2$  images captured by distinct cameras. The epipolar graph describes the relationships among all possible pairs of cameras in the set. The field of view of some camera pairs will partially overlap. In these cases, a relationship can be defined between the cameras, synthesized in the fundamental matrix  $F$  (or the essential matrix  $E$ ) characteristic of the pair. Other pairs of cameras will observe completely different scenes, and thus, no relationship can be found between them. Figure 4.24 illustrates a graphical representation of the epipolar graph.

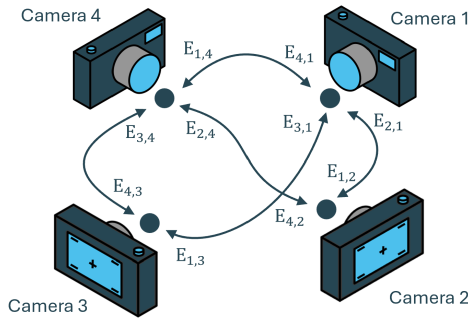


Figure 4.24: Epipolar Graph Graphical Representation

Each node of the epipolar graph represents a camera. Each edge represents the relationship between the two nodes it connects. Thus, each edge of the graph is described by a fundamental matrix  $F$  or, if the camera's intrinsic parameters are known, by an essential matrix  $E$ . More precisely, each pair of cameras can be associated with two branches of the epipolar graph. During the stereo calibration, two fundamental (or essential) matrices can be computed for each camera pair. For instance, for cameras 1 and 2, both the fundamental matrix connecting the points of camera 2 to those of camera 1,  $F_{2,1}$ , and the fundamental matrix connecting the points of camera 1 to those of camera 2,  $F_{1,2}$ , can be calculated. Since these

matrices derive from different stereo calibrations, matrix  $F_{2,1}$  is not simply the transpose of  $F_{1,2}$ . These minor differences provide additional valuable information for optimizing the multicamera system and must be fully exploited to enhance the reliability and accuracy of 3D reconstruction.

#### 4.2.3.2 Theoretical Aspects

Numerous techniques exist to fully use the information in the epipolar graph and achieve optimal multi-camera calibration. These techniques aim to describe all the perspective matrices of the system cameras relative to a common reference frame.

In this thesis, a well-known approach called Camera Synchronization was chosen to initialize the perspective matrices. Subsequently, they were optimized using a technique called Bundle Block Adjustment. The following briefly describes the fundamental principles of the employed techniques. For a more formal and comprehensive explanation, we refer the reader to the specialized texts used (R. Hartley and Zisserman 2003, Fusiello 2005).

Camera synchronization is based on a network of relative transformations between different reference frames. This method allows for initialising each perspective matrix of the system cameras relative to a common reference frame. Therefore, it is necessary to decide which reference frame to use for the perspective matrices. Similar to stereo calibration, it is convenient to use the reference frame of a single camera as the primary reference frame. In a system comprising  $m \geq 3$  cameras, the reference frame of camera 1 is designated as the primary reference frame. Each of the perspective matrices  $P_i$  can then be expressed using Equation 4.38.

$$P_i = K_i[R_i \mid T_i] \quad (4.38)$$

In which  $R_i$  and  $T_i$  denote, respectively, the rotation ( $R_{i,1}$ ) and translation ( $T_{i,1}$ ) from the reference frame of camera  $i$  to that of camera 1.

Generally, the relative rotation and translation from the  $i$ -th camera reference frame to the first camera cannot be directly determined. This is because there is no guaranteed overlap between the scene observed by camera  $i$  and that captured by camera 1. Therefore, the relative rotation-translation ( $R_i \mid T_i$ ) must be computed by composing relative orientations. By examining an epipolar graph (Figure 4.24), it can be observed that more than one path can be followed to express the rotation-translation ( $R_i \mid T_i$ ). Synchronization implements a globally adapted solution that considers all available orientations as edges of the epipolar graph.

First, synchronization focuses on defining the angular orientation of each camera. This corresponds to calculating the rotation matrix  $R_i$  for each camera in the system. The  $R_i$  matrices must satisfy the compatibility equation 4.39 for the pair  $(i, j)$  available.

$$R_{i,j} = R_i R_j^T \quad (4.39)$$

This problem is widely known in the literature as rotation averaging (R. I. Hartley et al. 2013) or rotation synchronization (Singer 2011). From a mathematical perspective, it can be synthesized as a minimization problem expressed by Equation 4.40.

$$\min_{R_1, \dots, R_m \in SO(3)} \sum_{(i,j)} \|R_{ij} - R_i R_j^T\|_F^2. \quad (4.40)$$

This implies finding rotations that minimize the sum of errors between the observed relative rotations ( $R_{ij}$ ) and those calculated using the estimated rotations ( $R_i R_j^T$ ). To solve this minimization problem, the spectral decomposition of a matrix containing all the relative rotations is typically employed. The matrix of relative rotations is usually denoted by  $Z$  and assumes the form shown in Equation 4.41.

$$Z = \begin{bmatrix} I & R_{1,2} & \cdots & R_{1,m} \\ R_{2,1} & I & \cdots & R_{2,m} \\ \vdots & \vdots & \ddots & \vdots \\ R_{m,1} & R_{m,2} & \cdots & I \end{bmatrix}. \quad (4.41)$$

In a practical scenario, not all relative rotations are typically available; in such cases, the blocks of  $Z$  corresponding to unknown rotations are set to zero. The first column of  $Z$  contains the rotations that describe the reference frames of all cameras with respect to the first camera one. Usually, this column is called the matrix  $X = [R_1, R_2, \dots, R_m]^T$  and contains the unknowns of the problem.

Since  $Z$  is a symmetric matrix, it can be written as  $Z = XX^T$ . Multiplying both sides of this equation by  $X$  and recognising that  $X^T X = mI$ , the eigenvalues problem are obtained as stated in Equation 4.42.

$$ZX = mX \quad (4.42)$$

Applying graph theory, this problem can be rewritten as shown in Equation 4.43.

$$ZX = (D \otimes I_3)X \quad (4.43)$$

In this,  $D$  denotes the matrix of degrees of the epipolar graph, which contains the degree of the graph nodes on its diagonal.

In an ideal case, the columns of matrix  $X$  constitute the three eigenvectors of  $(D \otimes I)^{-1}Z$  corresponding to the eigenvalue one, while the other eigenvalues are zero. In practice, this generally does not occur. For this reason, the eigenvectors associated with the dominant eigenvalues are taken.

Finally, to ensure that the estimated rotations are indeed valid rotations (i.e., belong to the special orthogonal group  $SO(3)$ ), the obtained solution is projected onto the  $SO(3)$  group, providing the closest rotation matrix.

Once the rotation matrices are written with respect to a common reference frame, the same procedure can be applied to the translation vectors. In the case of translation, the compatibility condition to be satisfied is expressed by Equation 4.44.

$$T_{i,j} = R_i((-R_j^T T_j) - (-R_i^T T_i)) = R_i(\tilde{C}_j - \tilde{C}_i) \quad (4.44)$$

This can be expressed in the form of Equation 4.45.

$$R_i^T T_{i,j} = \tilde{C}_j - \tilde{C}_i = u_{i,j} \quad (4.45)$$

In which  $\tilde{C}_i$  denotes the centre of the  $i$ -th camera (in Cartesian coordinates), and  $u_{i,j}$  represents the translation written with respect to the global reference frame (i.e., expressed relative to the reference frame of the first camera).

The solution to this problem again derives from graph theory. As with the previous case, a matrix  $X$  is introduced, containing the centres of each camera juxtaposed:  $X = [\tilde{C}_1 \quad \tilde{C}_2 \quad \dots \quad \tilde{C}_m]$ . Utilizing this matrix, Equation 4.45 can be rewritten as shown in Equation 4.46.

$$Xb_{i,j} = u_{i,j} \quad (4.46)$$

Where the vector  $b_{i,j}$  (shown in Equation 4.47) represents a edge of the epipolar graph and, in terms of graph theory, can be seen as a column of the incidence matrix.

$$b_{ij} = (0, \dots, \underset{i}{-1}, \dots, \underset{j}{1}, \dots, 0)^\top \quad (4.47)$$

Equation 4.46 can be written in matrix form (as shown in Equation 4.48), introducing the incidence matrix.

$$XB = U \quad (4.48)$$

In which  $B$  is the incidence matrix ( $m \times l$ , where  $l$  is the number of edges of the epipolar graph). While  $U$  ( $3 \times l$ ) is the matrix that has the vectors  $u_{i,j}$  as columns.

Aligning the global reference frame with the first camera's one lead to have  $\tilde{C}_1 = 0$ . By imposing this constraint, the first row of matrix  $B$  can be removed. This new matrix is  $B_1$  ( $(m - 1) \times l$ ). This step transitions from matrix  $B$ , which has a maximum rank of  $m - 1$ , to matrix  $B_1$ , which has a maximum rank.

At this point, by vectorizing Equation 4.48, we obtain a set of equations that allow us to compute all the components of matrix  $X$  (Equation 4.49).

$$(B_1^\top \otimes I) \text{vec}(X_1) = \text{vec}(U) \quad (4.49)$$

Obviously, as in the previous case, this equation represents an overdetermined problem, which generally does not have an analytical solution. It can be demonstrated that, among all solutions satisfying the compatibility constraints, the least squares solution is the closest to the measurements in the Euclidean norm.

At this point of the discussion, the projection matrices of each camera ( $P_i$ ) have been expressed within a standard reference frame. Furthermore, the computation of these matrices has accounted for all the relative orientations among the cameras using the information in the epipolar graph. Despite this, the solution thus obtained is not statistically optimal. This method, indeed, ignores all the information contained in the positions of the points, which have only contributed to determining the relative orientation between pairs of images.

A truly global method should optimize a cost function that simultaneously incorporates all images and all tie points.

The bundle block adjustment is an optimization procedure that minimizes the overall reprojection error of tie points in the images where they are visible relative to their 3D coordinates and the cameras' parameters (both internal and external).

From a practical perspective, minimizing the reprojection error means to solve a complex minimization problem.

Consider a series of world points  $M^j$ , where  $j = \dots n$ . Each point can be projected onto the image plane of the  $i$ -th camera according to the relation  $P_i M^j$ . The distance between the point measured on the image plane,  $m_i^j$ , and its projection through the camera model,  $P_i M^j$ , constitutes the reprojection error associated with

that point and that camera. The bundle block adjustment aims to minimize the sum of the squared distances between the  $j$ -th point reprojected by the  $i$ -th camera for every image in which the point appears. Equation 4.50 shows the cost function of the problem.

$$\chi(M^j, P_i) = \sum_{i=1}^m \sum_{j=1}^n \|\tilde{\eta}(P_i M^j) - m_{ij}\|^2 \quad (4.50)$$

Where  $\tilde{\eta}$  is a function referred to as the perspective division (Equation 4.51).

$$\tilde{\eta} : \mathbb{R}^3 \rightarrow \mathbb{R}^2, \quad \tilde{\eta}([x, y, z]^\top) = \begin{bmatrix} x \\ z \end{bmatrix}^\top \quad (4.51)$$

This problem is highly nonlinear and involves a significant number of degrees of freedom. Specifically, it requires the simultaneous adjustment of both the  $m$  cameras and the  $n$  connection points. Each camera has ten degrees of freedom, while each point contributes three more. This results in a cost function with numerous local minima. To ensure that the calibration process is robust and reliable, using the projective matrices  $P_i$  obtained from camera synchronization as the starting point is essential. This approach ensures that the initial configuration is close to the global minimum, thereby guaranteeing the calibration process's success.

#### 4.2.3.3 Accuracy Validation

The complexity of synchronization and adjustment processes in multiview calibration requires verification of the obtained results to ensure their reliability. The Bundle Block Adjustment is based on minimizing the reprojection error. However, a reduced reprojection error does not necessarily guarantee an accurate calibration model. Indeed, if the Bundle Block Adjustment converges to a local minimum, the resulting model may not adequately represent reality. For this reason, it is essential to consider the multicamera system's triangulation performance.

This thesis employed a three-camera system. Two indicators were observed to ensure the reliability of the calibration for this system. Three stereo pairs are obtained by expressing all the system's projection matrices relative to the reference frame of the first camera. As done for stereo calibration, it is possible to evaluate the performance of each stereo pair by analyzing the metrics reported in Table 4.5.

	Cam 1 - Cam 2	Cam 1 - Cam 3	Cam 2 - Cam 3
Mean [%]	0.057	0.047	0.036
Max [%]	3.750	3.078	3.33
Std. Dev.	0.914	0.723	0.829
Skewness	-0.034	0.381	0.213
Kurtosis	0.520	0.883	0.221
Outliers [%]	0.542	0.813	0.135

Table 4.5: Triangulation Metrics for both the Stereo Rig in a Multiview Calibration

Even if each dipole produces good triangulation results, this does not ensure that the entire system is correctly oriented and calibrated. For this reason, the distances between points in the world space were analyzed by projecting homologous

points through dipoles of different cameras. Figure 4.25 shows the distributions of the distances between homologous points triangulated using different stereo dipoles.

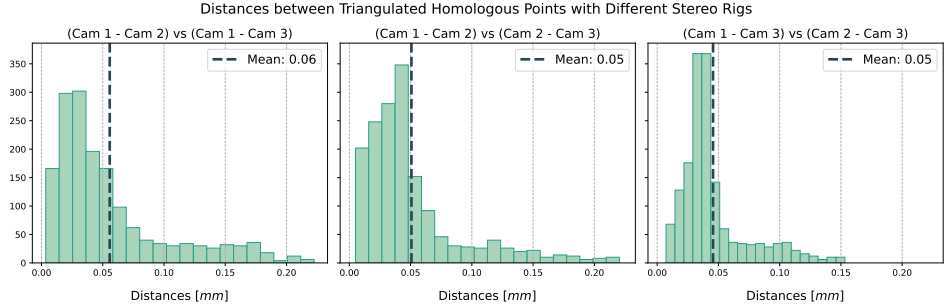


Figure 4.25: Statistical Distributions of Distances between Triangulated Homologous Points with Different Stereo Rigs

Examining these distributions and the associated metric values (Table 4.6) makes it possible to ensure the successful outcome of the multi-camera calibration.

	Cam 1 - Cam 2 vs Cam 1 - Cam 3	Cam 1 - Cam 2 vs Cam 2 - Cam 3	Cam 1 - Cam 3 vs Cam 2 - Cam 3
Mean [mm]	0.056	0.051	0.046
Max [mm]	0.223	0.220	0.153
Std. Dev.	0.047	0.041	0.028

Table 4.6: Metrics of Distributions of Distances between Triangulated Homologous Points with Different Stereo Rig Configurations

## 4.3 Reconstruction Strategies

This section presents the three-dimensional reconstruction techniques used in this thesis. Specifically, the focus is on these methods' theoretical aspects and potential applications. The challenges encountered and the solutions adopted for their practical implementation will instead be discussed in detail within the chapters dedicated to the case studies (Chapter ??, Chapter ??). Specifically, this thesis explores two three-dimensional reconstruction methods: stereo triangulation and shape from the silhouette. Both techniques were selected for their specific characteristics, making them complementary in the context of analysed case studies.

### 4.3.1 Stereo Triangulation

The literature contains a large number of triangulation algorithms. The algorithm used in this thesis is known as the linear triangulation method. This algorithm is by far among the most widely used triangulation techniques. It guarantees good

accuracy with low complexity. The popularity of this technique also makes it appealing from an implementation perspective. Various programming libraries, such as OpenCV (OpenCV 2024), provide optimized implementations of this algorithm, facilitating the development of practical applications.

When a point in three-dimensional space,  $M$ , is observed by a camera, its projection  $m$  onto the image plane defines a visual ray. This ray originates from the camera's optical centre,  $\omega$ , and passes through the projected point on the image plane. Given the camera's perspective projection matrix ( $PPM$ ) and the coordinates of the point  $m$ , it is possible to project the visual ray into 3D space. However, it is impossible to determine the point  $M$  coordinates directly. For this reason, triangulation requires using at least two cameras (1 and 2) in a stereo configuration.

In such a framework, the projections  $m_1$  and  $m_2$  of a 3D point  $M$  onto the respective image planes are described by Equation 4.52.

$$m_i = PPM_i M \quad i = 1, 2 \quad (4.52)$$

Where  $M = [X, Y, Z, 1]$  denotes the homogeneous coordinates of the three-dimensional point. While,  $m_i = [u_i, v_i, 1]$  denotes the homogeneous coordinates of the projection of  $M$  onto the image plane of the  $i$ -th camera. Finally,  $PPM_i$  denotes the  $i$ -th perspective matrix obtained during calibration.

As shown in Figure 4.26, by knowing the perspective matrices of two or more cameras and the projections of a point on the respective images, it is possible to determine the three-dimensional coordinates of that point. Two visual rays can be drawn using the Equation 4.52. The intersection of these rays defines the coordinates of the point in three-dimensional space.

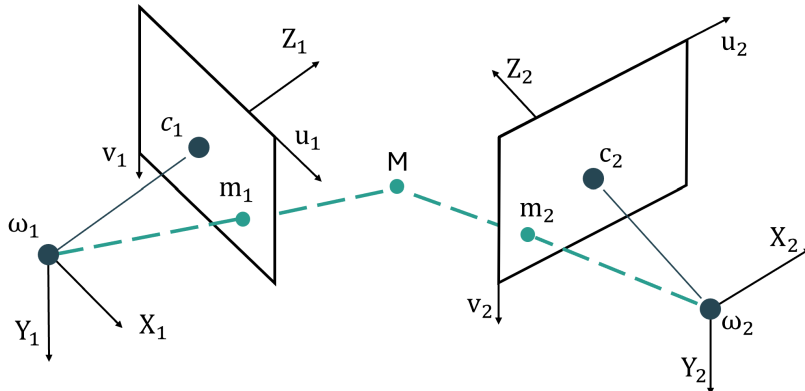


Figure 4.26: Stereo Triangulation by Visual Beams Intersection

From a mathematical perspective, finding the intersection of visual rays corresponds to solving a linear system. To define this system, it is first necessary to develop Equation 4.52, as shown in Equation 4.53.

$$\begin{cases} u = {}^1PPM M \\ v = {}^2PPM M \\ 1 = {}^3PPM M \end{cases} \rightarrow \begin{cases} ({}^1PPM - u {}^3PPM)^T M = 0 \\ ({}^2PPM - v {}^3PPM)^T M = 0 \end{cases} \quad (4.53)$$

Here,  ${}^n PPM$  represents the  $n$ -th row of the perspective projection matrix of the camera. Each camera, therefore, provides two equations, which correspond to the Cartesian representation of the visual ray. By combining at least two visual rays into a system, we obtain Equation 4.54, which allows the calculation of the world coordinates of the point  $M$ . By introducing the matrix  $A$ , which collects the various perspective rays, the problem can be rewritten in matrix form.

$$\begin{cases} ({}^1 PPM_1 - u_1 {}^3 PPM_1)^T M = 0 \\ ({}^2 PPM_1 - v_1 {}^3 PPM_1)^T M = 0 \\ ({}^1 PPM_2 - u_2 {}^3 PPM_2)^T M = 0 \\ ({}^2 PPM_2 - v_2 {}^3 PPM_2)^T M = 0 \end{cases} \rightarrow A M = 0 \quad (4.54)$$

Although this approach is highly robust, achieving good results requires careful consideration of some key factors. First, it is essential to correct the positions of the homologous points  $m_1$  and  $m_2$  by applying the most suitable distortion model to eliminate lens-induced effects. Additionally, if necessary, the homographies ( $H_1$  and  $H_2$ ) should be applied to account for the deformation of the tunnel windows. This process ensures that the point coordinates are corrected for optical aberrations.

Accurately identifying homologous points in different images is a complex challenge in practical cases. Due to the discrete nature of digital images, locating exact projections of the same point in three-dimensional space is basically impossible. These uncertainties are further compounded by the inherent inaccuracies of the perspective matrices. Even minor errors in these matrices can have significant effects, often preventing the intersection of the projective rays associated with homologous points. Mathematically, this results in the inability to analytically solve Equation 4.54.

Observing Equation 4.54, it is evident that two visual rays provide four constraints. However, determining the position of a point in three-dimensional space requires only three coordinates, making the system overdetermined. The solution to this problem is typically obtained using a least-squares approach, frequently using a singular value decomposition (SVD). Adding additional cameras to the system can significantly enhance the accuracy of the 3D reconstruction. Each new camera introduces two additional constraints to Equation 4.54, thereby increasing the robustness of the overall solution. A larger number of constraints enables a more precise estimation of the position of the point  $M$  and ensures higher reliability of the measurement system.

Finally, it is important to consider the sensitivity of Equation 4.54 to noise. The matrix  $A$  contains terms with significantly different orders of magnitude. This occurs because, when expressing image point coordinates in homogeneous form, the first two components are typically much larger than the third. Furthermore, depending on how the world reference system is defined, the projection matrices may have components with differing orders of magnitude. These differences make the matrix  $A$  ill-conditioned and, therefore, sensitive to noise. For this reason, a data preconditioning procedure is usually applied. This procedure involves introducing an affine transformation  $T$  to reformulate the projection matrices, as shown in Equation 4.55.

$$P\hat{P}M = T PPM \quad (4.55)$$

Here,  $P\hat{P}M$  represents the well-conditioned perspective projection matrix. The

elements of the matrix  $T$  allow for translating and scaling the coordinates of the image points so that they have comparable magnitudes. A common form of the matrix  $T$  is provided in Equation 4.56.

$$T = \begin{pmatrix} \frac{\sqrt{2}}{d} & 0 & -g_x \\ 0 & \frac{\sqrt{2}}{d} & -g_y \\ 0 & 0 & 1 \end{pmatrix} \quad (4.56)$$

The components of this matrix must be calculated based on the group of points to be triangulated. Considering a group of  $n$  points ( $m^j = [u^j, v^j, 1]^T$   $j = 1, \dots, N$ ) on the image plane, the components of  $T$  can be expressed using Equation 4.57.

$$\begin{cases} g_x = \frac{1}{N} \sum_{j=1}^N u_i, \\ g_y = \frac{1}{N} \sum_{j=1}^N v_i, \\ d = \frac{1}{N} \sum_{j=1}^N \sqrt{(u_i - g_x)^2 + (v_i - g_y)^2}. \end{cases} \quad (4.57)$$

Preconditioning produces normalized points that satisfy two fundamental properties: their centroid is located at the origin of the coordinate system, and the average distance of the points from the origin is  $\sqrt{2}$ . These conditions ensure that the numerical values in matrix  $A$  are well-balanced, reducing the effects of minor errors and improving the stability of singular value decomposition.

Triangulation techniques can be divided into two categories: active and passive triangulation. Active triangulation involves using external markers to simplify the identification of corresponding points in images captured by different cameras. These markers can include laser projections, structured light patterns, or printed patterns on the object, such as grids or point series. On the other hand, passive triangulation relies solely on the geometric and chromatic characteristics of the object to be reconstructed without the need for external markers. In this case, the identification of corresponding points between camera images is achieved through feature recognition (i.e., pixels or areas easily identified and matched in different images).

### 4.3.2 Shape from Silhouette

Shape from silhouette is a technique for reconstructing an object's three-dimensional shape from silhouettes observed from multiple viewpoints. This approach utilizes the geometric information the silhouettes provide to generate a 3D volume approximating the object's overall form, known as the visual hull. The theoretical principle behind this technique is based on the intersection of visual cones, defined by the projected silhouettes in 3D space. Each image captures the object's shape from a specific viewpoint, representing its silhouette. Visual cones are generated by projecting these silhouettes along the camera's perspective rays. The intersection of these cones provides an approximation of the object's three-dimensional volume. A representative diagram of the shape from the silhouette is shown in figure 4.27.

From a practical standpoint, applying the shape-by-silhouette technique first requires considering a volume in three-dimensional space. This volume is typically discretized into a voxel grid, which consists of a set of three-dimensional points, each associated with a small volume.

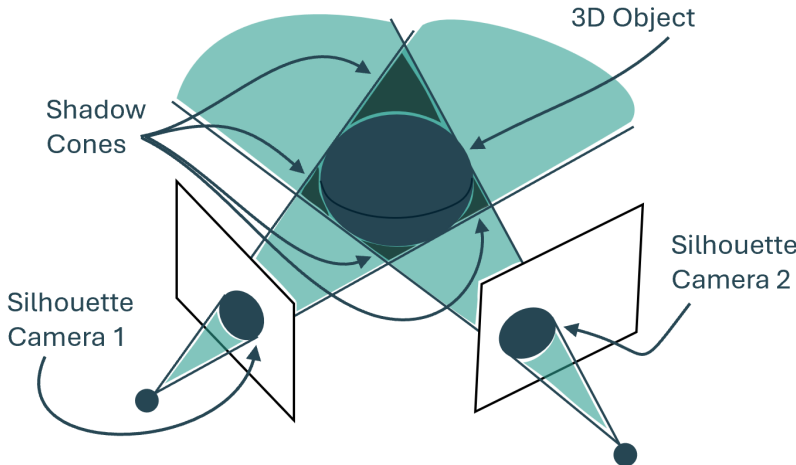


Figure 4.27: Visual Cones Intersection in Shape by Silhouette

Using Equation 4.9, each voxel can be projected onto the image plane of a specific camera. By comparing this projection with the object's silhouette as seen from the camera, it is possible to determine which voxels belong to the object and which do not. Consequently, the initial voxel grid is refined by eliminating any voxels that correspond to pixels outside the object's silhouette when projected onto the image plane. This process, known as 'carving', allows the volumetric representation to be restricted within the limits defined by the observed silhouette. Obviously, using a single camera leads to a very coarse three-dimensional reconstruction of the object. This occurs because all points in three-dimensional space that project within the silhouette on the image plane are considered part of the object, including those that belong to the shadow cones created by perspective. Additional cameras observing the object from different viewpoints are necessary to achieve a better reconstruction. This reduces the size of the shadow cones, progressively enhancing the precision of the object's carving.

Even in this context, it is important to consider optical distortions caused by the lenses and distortions caused by tunnel window bending. However, in this case, applying the calculated corrections to the reprojected points would be very inconvenient. Indeed, it would be necessary to invert both the distortion models and, when used, the homographies. Inverting these relationships is not straightforward. For example, homographies often suffer from poor conditioning, necessitating a procedure similar to that discussed in Section 4.3.1.

For this reason, it is preferable to correct the coordinates of the silhouette points and then compare these with the voxel projections on the image planes directly. This ensures that both distortion models and homographies are applied straightforwardly.

Compared to stereo triangulation, this technique has advantages and disadvantages. On the one hand, the implementation is considerably simpler, as it does not require identifying and matching homologous points between images from different cameras. It is sufficient to segment the object's edges to be reconstructed, a generally less complex task. On the other hand, however, the effective use of this

technique is not trivial. For the visual hull to represent a good approximation of the real object, obtaining an extremely accurate silhouette segmentation is essential. Furthermore, an accurate reconstruction requires a sufficient number of views of the object taken from different angles. In a cavitation tunnel, the number of available cameras is often limited due to the high cost of the instrumentation and the restrictions of optical access to the test section. For this reason, the viewing angles must be chosen with great care to maximise the quality of the reconstruction.

# Bibliography

- Arabnejad, Mohammad Hossein et al. (2020). "Hydrodynamic Mechanisms of Aggressive Collapse Events in Leading Edge Cavitation". In: *Journal of Hydrodynamics* 32, pp. 6–19. DOI: [10.1007/s42241-020-0002-8](https://doi.org/10.1007/s42241-020-0002-8).
- Bosschers, Johan (2018). "A Semi-Empirical Prediction Method for Broadband Hull-Pressure Fluctuations and Underwater Radiated Noise by Propeller Tip Vortex Cavitation". In: *Journal of Marine Science and Engineering* 6.2. ISSN: 2077-1312. DOI: [10.3390/jmse6020049](https://doi.org/10.3390/jmse6020049). URL: <https://www.mdpi.com/2077-1312/6/2/49>.
- Brennen, C.E. (2014). *Cavitation and Bubble Dynamics*. Cavitation and Bubble Dynamics. Cambridge University Press. ISBN: 9781107644762. URL: <https://books.google.it/books?id=yRhaAQAAQBAJ>.
- Brennen, Christopher (1970). "Cavity Surface Wave Patterns and General Appearance". In: *Journal of Fluid Mechanics* 44, pp. 33–49. DOI: [10.1017/S0022112070001672](https://doi.org/10.1017/S0022112070001672).
- Brown, N. A. (1999). "Thruster Noise". In.
- Capone, Alessandro, Francisco Alves Pereira, and Fabio Di Felice (2024). "Flow and Cavity Measurements in a Super-Cavitating Propeller". In: *Journal of Marine Science and Engineering* 12.2. ISSN: 2077-1312. DOI: [10.3390/jmse12020243](https://doi.org/10.3390/jmse12020243). URL: <https://www.mdpi.com/2077-1312/12/2/243>.
- Carlton, J. (2018). *Marine Propellers and Propulsion*. Butterworth-Heinemann. ISBN: 9780081003749. URL: <https://books.google.it/books?id=2drWDgAAQBAJ>.
- Ceccio, S. L. and C. E. Brennen (1991). "Observations of the Dynamics and Acoustics of Travelling Bubble Cavitation". In: *Journal of Fluid Mechanics* 233, pp. 633–660. DOI: [10.1017/S0022112091000630](https://doi.org/10.1017/S0022112091000630).
- Chizelle, Y. et al. (1994). "Cavitation Scaling Experiments With Headforms: Bubble Acoustics". In.
- De Chizelle, Y. Kuhn, S. L. Ceccio, and C. E. Brennen (1995). "Observations and Scaling of Travelling Bubble Cavitation". In: *Journal of Fluid Mechanics* 293, pp. 99–126. DOI: [10.1017/S0022112095001650](https://doi.org/10.1017/S0022112095001650).
- Dular, Matevž and Olivier Coutier-Delgosha (2009). "Numerical Modelling of Cavitation Erosion". In: *International Journal for Numerical Methods in Fluids* 61.12, pp. 1388–1410. DOI: <https://doi.org/10.1002/fld.2003>. eprint: <https://onlinelibrary.wiley.com/doi/pdf/10.1002/fld.2003>. URL: <https://onlinelibrary.wiley.com/doi/abs/10.1002/fld.2003>.
- Ebert, Eric and Nils Damaschke (2019). "Synchronized Multi-camera and LED-illumination system for multi perspective cavitation observation and 3D reconstruction". In: URL: <https://api.semanticscholar.org/CorpusID:247586244>.

- Fischler, Martin A. and Robert C. Bolles (1981). "Random sample consensus: a paradigm for model fitting with applications to image analysis and automated cartography". In: *Commun. ACM* 24, pp. 381–395. URL: <https://api.semanticscholar.org/CorpusID:972888>.
- Franc, J.P. and J.M. Michel (2006). *Fundamentals of Cavitation*. Fluid Mechanics and Its Applications. Springer Netherlands. ISBN: 9781402022333. URL: [https://books.google.it/books?id=QJOQYa\\_oo24C](https://books.google.it/books?id=QJOQYa_oo24C).
- Franzosi, Giovanni et al. (June 2023). "Analysis of Blade Root Cavitation Erosion with an Image Processing Approach". In: 33th International Ocean and Polar Engineering Conference, ISOPE-I-23-588. eprint: <https://onepetro.org/ISOPEIOPEC/proceedings-pdf/ISOPE23/A11-ISOPE23/ISOPE-I-23-588/3164627/isope-i-23-588.pdf>.
- Fusiello, Andrea (2005). "Elements of Computer Vision : Multiple View Geometry". In: URL: <https://api.semanticscholar.org/CorpusID:11746387>.
- Hammitt, F. G. (Sept. 1963). "Observations on Cavitation Damage in a Flowing System". In: *Journal of Basic Engineering* 85.3, pp. 347–356. ISSN: 0021-9223. DOI: [10.1115/1.3656601](https://doi.org/10.1115/1.3656601). eprint: [https://asmedigitalcollection.asme.org/fluidsengineering/article-pdf/85/3/347/5494326347\\_1.pdf](https://asmedigitalcollection.asme.org/fluidsengineering/article-pdf/85/3/347/5494326347_1.pdf). URL: <https://doi.org/10.1115/1.3656601>.
- Hartley, R. and A. Zisserman (2003). *Multiple View Geometry in Computer Vision*. Cambridge books online. Cambridge University Press. ISBN: 9780521540513. URL: <https://books.google.it/books?id=si3R3Pfa98QC>.
- Hartley, Richard I. et al. (2013). "Rotation Averaging". In: *International Journal of Computer Vision* 103, pp. 267–305. URL: <https://api.semanticscholar.org/CorpusID:10021879>.
- International Maritime Organization (IMO) (July 2023). *80th Session of the Marine Environment Protection Committee (MEPC 80)*. Adopted strategies on GHG emissions, biofouling management, underwater noise reduction, and ballast water management. URL: <https://www.imo.org/en/MediaCentre/WhatsNew/Pages/default.aspx>.
- ITTC (2011). "Recommended Procedures and Guidelines - Cavitation Induced Erosion on Propellers, Rudders and Appendages Model Scale Experiments". In: pp. 1–14. URL: <https://www.ittc.info/media/8043/75-02-03-035.pdf>.
- Kermeen, Robert W. (1956). "Water Tunnel Tests of NACA 4412 and Walchner Profile 7 Hydrofoils in Noncavitating and Cavitating Flows". In: URL: <https://api.semanticscholar.org/CorpusID:107349122>.
- Knapp, R.T., J.W. Daily, and F.G. Hammitt (1970). *Cavitation*. Engineering Societies Monographs. McGraw-Hill. URL: <https://books.google.it/books?id=T-hRAAAAMAAJ>.
- Köksal, Çağatay Sabri et al. (2021). "Numerical prediction of cavitation erosion to investigate the effect of wake on marine propellers". In: *Ocean Engineering* 239, p. 109820. ISSN: 0029-8018. DOI: <https://doi.org/10.1016/j.oceaneng.2021.109820>. URL: <https://www.sciencedirect.com/science/article/pii/S0029801821011793>.
- Kuiper, G. (1998). "Cavitation Research and Ship Propeller Design". In: *In Fascination of Fluid Dynamics: A Symposium in Honour of Leen van Wijngaarden*. Ed. by Arie Biesheuvel and Gertjan F. van Heijst. Dordrecht: Springer Netherlands, pp. 33–50. ISBN: 978-94-011-4986-0. DOI: [10.1007/978-94-011-4986-0\\_3](https://doi.org/10.1007/978-94-011-4986-0_3). URL: [https://doi.org/10.1007/978-94-011-4986-0\\_3](https://doi.org/10.1007/978-94-011-4986-0_3).

- Kuiper, Gert (1981). "Cavitation inception on ship propeller models". In: URL: <https://api.semanticscholar.org/CorpusID:122569530>.
- Lamb, H. (1932). "Hydrodynamics. 6th edition". In: URL: <https://books.google.it/books?id=n0HRXwAACAAJ>.
- Leclercq, Christophe et al. (2017). "Numerical Cavitation Intensity on a Hydrofoil for 3D Homogeneous Unsteady Viscous Flows". In: *International Journal of Fluid Machinery and Systems* 10, pp. 254–263. URL: <https://api.semanticscholar.org/CorpusID:116120807>.
- Lecoffre, Y. (1999). *Cavitation: Bubble Trackers*. Taylor & Francis. ISBN: 9789054107835. URL: [https://books.google.it/books?id=\\_In\\_M-yBYtMC](https://books.google.it/books?id=_In_M-yBYtMC).
- Lighthill, M. J. (1952). "On Sound Generated Aerodynamically. I. General Theory". In: *Proceedings of the Royal Society of London. Series A, Mathematical and Physical Sciences* 211.1107, pp. 564–587. ISSN: 00804630. URL: <http://www.jstor.org/stable/98943> (visited on 11/21/2024).
- Lindgren, Hans (1966). "Cavitation Inception on Head Forms ITTC Comparative Experiments". In: URL: <https://api.semanticscholar.org/CorpusID:204305944>.
- Lloyd, Thomas et al. (Nov. 2020). *Progress in the prediction and mitigation of propeller cavitation noise and vibrations*.
- Louhichi, H et al. (July 2007). "Self-calibration of Scheimpflug cameras: an easy protocol". In: *Measurement Science and Technology* 18.8, p. 2616. DOI: <10.1088/0957-0233/18/8/037>. URL: <https://dx.doi.org/10.1088/0957-0233/18/8/037>.
- Mantzaris, Anastasios et al. (Sept. 2015). "ESTABLISHMENT AND VERIFICATION OF REPRODUCIBLE METHOD FOR COATING PROPELLER BLADES FOR EROSIVE CAVITATION DETECTION". In.
- Melissaris, Themistoklis et al. (2020). "On the accuracy of predicting cavitation impact loads on marine propellers". In: *Wear* 456-457, p. 203393. ISSN: 0043-1648. DOI: <https://doi.org/10.1016/j.wear.2020.203393>. URL: <https://www.sciencedirect.com/science/article/pii/S0043164819316679>.
- OpenCV (2024). *OpenCV - Open Source Computer Vision Library*. <https://opencv.org>. Accessed: 2024-12-18.
- Pennings, P. C., J. Westerweel, and T. J. C. van Terwisga (Nov. 2015). "Flow field measurement around vortex cavitation". In: *Experiments in Fluids* 56.11, p. 206. ISSN: 1432-1114. DOI: <10.1007/s00348-015-2073-9>. URL: <https://doi.org/10.1007/s00348-015-2073-9>.
- Pereira, F., F. Avellan, and Ph. Dupont (Dec. 1998). "Prediction of Cavitation Erosion: An Energy Approach". In: *Journal of Fluids Engineering* 120.4, pp. 719–727. ISSN: 0098-2202. DOI: <10.1115/1.2820729>. eprint: [https://asmedigitalcollection.asme.org/fluidsengineering/article-pdf/120/4/719/5900617/719\\_1.pdf](https://asmedigitalcollection.asme.org/fluidsengineering/article-pdf/120/4/719/5900617/719_1.pdf). URL: <https://doi.org/10.1115/1.2820729>.
- Peters, Andreas, Udo Lantermann, and Ould el Moctar (2018). "Numerical prediction of cavitation erosion on a ship propeller in model- and full-scale". In: *Wear* 408-409, pp. 1–12. ISSN: 0043-1648. DOI: <10.1016/j.wear.2018.04.012>. URL: <https://www.sciencedirect.com/science/article/pii/S0043164817316307>.
- Peters, Andreas, Hemant Sagar, et al. (2015). "Numerical modelling and prediction of cavitation erosion". In: *Wear* 338-339, pp. 189–201. ISSN: 0043-1648. DOI:

- <https://doi.org/10.1016/j.wear.2015.06.009>. URL: <https://www.sciencedirect.com/science/article/pii/S0043164815003415>.
- Pfitsch, Woody et al. (2009). "Development of Measurement Techniques for Studying Propeller Erosion Damage in Severe Wake Fields". In: URL: <https://api.semanticscholar.org/CorpusID:55093306>.
- Plessset, Milton S. and Richard B. Chapman (1971). "Collapse of an Initially Spherical Vapour Cavity in the Neighbourhood of a Solid Boundary". In: *Journal of Fluid Mechanics* 47, pp. 283–290. DOI: [10.1017/S0022112071001058](https://doi.org/10.1017/S0022112071001058).
- Proctor, Fred H. et al. (2010). "Three-Phased Wake Vortex Decay". In: URL: <https://api.semanticscholar.org/CorpusID:26695879>.
- Rojano-Doñate, Laia et al. (Sept. 2023). *Effect of Vessel Noise on Marine Mammals and Measures to Reduce Impact*, pp. 1–17. DOI: [10.1007/978-3-031-10417-6\\_138-1](https://doi.org/10.1007/978-3-031-10417-6_138-1).
- Ross, D. (2013). *Mechanics of Underwater Noise*. Elsevier Science. ISBN: 9781483160467. URL: <https://books.google.it/books?id=sdwgBQAAQBAJ>.
- Russell, Daniel A., Joseph P. Titlow, and Ya-Juan Bemmen (Aug. 1999). "Acoustic monopoles, dipoles, and quadrupoles: An experiment revisited". In: *American Journal of Physics* 67.8, pp. 660–664. ISSN: 0002-9505. DOI: [10.1119/1.19349](https://doi.org/10.1119/1.19349). eprint: [https://pubs.aip.org/aapt/ajp/article-pdf/67/8/660/7528251/660\\_1\\_online.pdf](https://pubs.aip.org/aapt/ajp/article-pdf/67/8/660/7528251/660_1_online.pdf). URL: <https://doi.org/10.1119/1.19349>.
- Savio, Luca, Michele Viviani, and Marco Ferrando (May 2011). "Application of computer vision techniques to measure cavitation bubble volume and cavitating tip vortex diameter". In.
- Schiebe, Frank R. (1972). "Measurement of the Cavitation Susceptibility of Water Using Standard Bodies". In: URL: <https://api.semanticscholar.org/CorpusID:137251372>.
- Schmidt, Steffen et al. (July 2008). "Numerical Analysis of Shock Dynamics for Detection of Erosion Sensitive Areas in Complex 3-D Flows". In.
- Sedlazeck, Anne and Reinhard Koch (2012). "Perspective and Non-perspective Camera Models in Underwater Imaging – Overview and Error Analysis". In: ed. by Frank Dellaert et al., pp. 212–242.
- Shiraishi, Koichiro et al. (2024). "Cavity shape measurement on propeller blade surface by combination line CCD camera measurement method". In: *Ship Technology Research*, pp. 1–13.
- Singer, A. (2011). "Angular synchronization by eigenvectors and semidefinite programming". In: *Applied and Computational Harmonic Analysis* 30.1, pp. 20–36. ISSN: 1063-5203. DOI: <https://doi.org/10.1016/j.acha.2010.02.001>. URL: <https://www.sciencedirect.com/science/article/pii/S1063520310000205>.
- Testa, C., S. Ianniello, and F. Salvatore (2018). "A Ffowcs Williams and Hawkings formulation for hydroacoustic analysis of propeller sheet cavitation". In: *Journal of Sound and Vibration* 413, pp. 421–441. ISSN: 0022-460X. DOI: <https://doi.org/10.1016/j.jsv.2017.10.004>. URL: <https://www.sciencedirect.com/science/article/pii/S0022460X17307186>.
- Usta, Onur and Emin Korkut (2019). "Prediction of cavitation development and cavitation erosion on hydrofoils and propellers by Detached Eddy Simulation". In: *Ocean Engineering* 191, p. 106512. ISSN: 0029-8018. DOI: <https://doi.org/10.1016/j.oceaneng.2019.106512>. URL: <https://www.sciencedirect.com/science/article/pii/S0029801819306523>.

- Vijayan, Anuja and P Pradeep Kumar (Aug. 2023). "Experimental characterization of cavitation zone and cavity oscillation mechanism transitions in planar cavitating venturis". In: *Physics of Fluids* 35.8, p. 083331. ISSN: 1070-6631. DOI: [10.1063/5.0161121](https://doi.org/10.1063/5.0161121). eprint: <https://pubs.aip.org/aip/pof/article-pdf/doi/10.1063/5.0161121/18096855/083331\1\5.0161121.pdf>. URL: <https://doi.org/10.1063/5.0161121>.
- Vogel, A and W Lauterborn (1988). "Acoustic transient generation by laser-produced cavitation bubbles near solid boundaries". In: *The Journal of the Acoustical Society of America* 84.2, pp. 719–731.
- Weng, J., P. Cohen, and M. Herniou (1992). "Camera calibration with distortion models and accuracy evaluation". In: *IEEE Transactions on Pattern Analysis and Machine Intelligence* 14.10, pp. 965–980. DOI: [10.1109/34.159901](https://doi.org/10.1109/34.159901).
- Williams, J. E. Ffowcs and D. L. Hawkings (1969). "Sound Generation by Turbulence and Surfaces in Arbitrary Motion". In: *Philosophical Transactions of the Royal Society of London. Series A, Mathematical and Physical Sciences* 264.1151, pp. 321–342. ISSN: 00804614. URL: <http://www.jstor.org/stable/73790> (visited on 11/21/2024).
- Zhang, Zhengyou (2000). "A flexible new technique for camera calibration". In: *IEEE Transactions on pattern analysis and machine intelligence* 22.11, pp. 1330–1334.